Charging, degassing and distribution of hydrogen in cast iron

Rui Wu, Johan Ahlström, Hans Magnusson,
Karin Frisk, Åsa Martinsson

Swerea KIMAB

May 2015

SKB

Charging, degassing and distribution of hydrogen in cast iron

Rui Wu, Johan Ahlström, Hans Magnusson,
Karin Frisk, Åsa Martinsson

Swerea KIMAB

This report concerns a study which was conducted for Svensk Kärnbränslehantering AB (SKB). The conclusions and viewpoints presented in the report are those of the authors. SKB may draw modified conclusions, based on additional literature sources and/or expert opinions.

A pdf version of this document can be downloaded from www.skb.se.

Abstract

Using an electrochemical charging method, hydrogen charging and degassing and simulations of hydrogen diffusion and degassing have been carried out on a ferritic nodular cast iron insert intended for use as the load-bearing part of canisters for long term disposal of spent nuclear fuel. Previous methods for sample preparation and for measurement and calculation of hydrogen content have been further developed and adopted to describe hydrogen profile in relation to depth. Hydrogen diffuses into the cast iron. The highest hydrogen content of 130 wtppm, in comparison to 1.7 wtppm for the as-received cast iron, appears at outer surface. Hydrogen content decreases rapidly with increasing depth into the cast iron and this trend can be expressed by a power law. The longer the charging time, the higher the hydrogen content deep inside the cast iron. Hydrogen does diffuse out of the cast iron. The longer the degassing time and the higher the degassing temperature, the more the hydrogen escapes from the cast iron down to a minimum of 2.9 wtppm. The diffusion equations can be used to describe hydrogen charging behaviour. Some assumptions have to be adopted to model the hydrogen transport into cast iron. The hydrogen profile in relation to depth has been simulated and well reproduced.

Contents

1 Introduction

A programme to handle nuclear waste has been operating in Sweden for many years (SKB 2010). The spent nuclear fuel is planned to be disposed of deep down in the bedrock by encapsulating in cast iron insert enclosed by a copper canister. The cast iron bears the load and the copper canister provides corrosion protection. It is essential that the cast iron insert maintains integrity under designed repository lifetime of at least 100,000 years.

After being placed in the repository, the cast iron insert will have to sustain external loads up to 15 MPa (SKB 2009) at elevated temperature up to about 100°C (Raiko 2005) during first thousands of years. In addition, it is not yet excluded that external and/or internal hydrogen sources can be present. It is estimated that a remaining quantity of up to 600 grams of water in the canister can corrode the iron and produce hydrogen gas in a quantity that is not negligible (SKB 2010). A combination of stress, temperature and presence of hydrogen will apparently increase the risk for stress corrosion cracking and hydrogen embrittlement. The latter has been actually reported worldwide for steel (Dayal and Parvathavarthini 2003).

Cast iron from trial fabrication of inserts has been creep tested at room temperature, 100°C and 125°C in air (in the absence of hydrogen) (Martinsson et al. 2010). The results demonstrate that the nodular cast iron exhibits logarithmic creep at these temperatures, meaning that creep strain rate tends to decrease to zero. Despite the fact that the stresses on the test bars are of the same order of magnitude as the yield stress, the greatest creep deformation measured is not larger than about 0.025% after 10,000 hours. Even with the safety assessment's timescale up to one million years, the creep in cast iron has a negligible effect on the properties of the canister.

However, presence of hydrogen combined with stress and temperature will alter the mechanical behaviour of the cast iron. In spite of the fact that hydrogen embrittlement in ductile (nodular) cast iron has been seldom reported, some limited studies are available. A study at Swerea KIMAB (Martinsson et al. 2009) on the effect of hydrogen on tensile and creep properties of a nodular cast iron showed that both tensile and creep properties, in terms of strength and ductility, were notably reduced, i.e. tensile ductility reduced by nearly 50%. Another study (Matsuno et al. 2012) on the effect of hydrogen on tensile behaviour of a ductile cast iron demonstrated that hydrogen-charging accelerated crack growth from graphite and the accelerated crack growth markedly reduced ductility. This is more pronounced at slower strain rate.

There are two established methods to introduce hydrogen into a metallic material; namely 1) thermal and 2) electrochemical charging. These two methods are widely applied and detailed in Nakahara and Okinaka (1988). In the earlier study (Martinsson et al. 2009), both methods were used to charge the hydrogen into the cast iron. It was concluded that the electrochemical charging is the most effective method for the cast iron.

The quantity of hydrogen that can be introduced into cast iron is closely related to the diffusion and solubility of hydrogen in the cast iron even though hydrogen is exceptionally mobile. The study (Martinsson et al. 2009) has shown that a hydrogen uptake in the cast iron can occur and that the uptake is highly dependent on the environment to which the cast iron insert is exposed. The results indicated also that the hydrogen introduced at the surface can permeate to the bulk.

Fundamental questions that relate to the control of hydrogen embrittlement and hydrogen-assisted cracking are the sources of hydrogen in cast iron, its content and the rate that hydrogen can permeate in and out during charging and/or degassing treatments. The solubility of hydrogen depends not only on temperature but also strongly on the defect structure of the lattice due to existence of different kinds of sites and traps such as dislocations, grain boundaries, interfaces and pores. A number of possible sites and traps for hydrogen are schematically illustrated in Figure 1-1. The sites and traps do not bind hydrogen permanently, but significantly retard its diffusion. Hydrogen embrittlement is also reversible because hydrogen can diffuse both into and out of the cast iron.
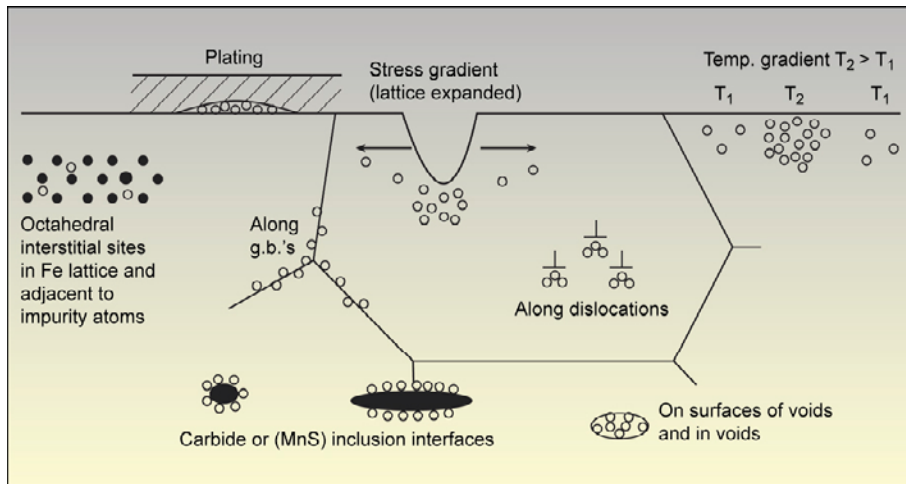
Figure 1-1. *Schematic illustration of sites and traps for hydrogen in steel. After Wanhill et al. (2011).*

2 Purposes of the project

The purposes of the present work are to

1) introduce hydrogen into a ferritic nodular cast iron in a controlled way,

2) develop and refine methods to measure, calculate and interpret hydrogen permeation depth profile,

3) establish a relation between hydrogen content and depth below subsurface,

4) investigate the role of pores for hydrogen uptaking and degassing,

5) use a simple model to simulate hydrogen diffusion and degassing and compare with experimental data to increase the understanding of the factors that influence hydrogen diffusion.

3 Diffusion of hydrogen in cast iron

3.1 Diffusion calculation

Diffusion of hydrogen in cast iron is usually modelled as diffusion of hydrogen in the matrix phase which is ferrite, and the presence of the possible sites and traps shown in Figure 1-1 is neglected. In this single-phase problem, a concentration gradient in hydrogen will lead to a flux of hydrogen atoms aiming to smoothen out this concentration gradient. The rate of this hydrogen transport is related to the steepness of the gradient and the size of the diffusion coefficient. This is expressed by Fick's law, with hydrogen flux J_H according to:

$$J_H = -D_H \cdot grad(c_H) \tag{3-1}$$

where D_H is the diffusion coefficient of hydrogen in iron, and c_H is the concentration of hydrogen in solid solution. Based on the conservation of mass, any changes in flux with time can expressed according to Fick's second law:

$$\frac{\partial c}{\partial t} = \frac{\partial}{\partial z}(D_H \cdot \frac{\partial c}{\partial z}) \tag{3-2}$$

Several different mathematical expressions exist for the mathematical solution of Fick's second law. In this work, an analytical solution will be used to get an estimate of the mechanisms ruling the hydrogen diffusion in iron. Then, a more detailed numerical method will be used to evaluate the hydrogen charging and degassing. This implies determining the concentration profile of hydrogen in iron as function of time during charging and degassing.

The choice of equation for analytical solution of Fick's second law depends on the boundary conditions of the considered problem. If a boundary is defined as a fixed concentration, which is often the case when a material is in equilibrium with a fixed activity, an erf-solution can be used. The time and distance dependency on the concentration profile is on the form:

$$c(z,t) = c_0(1 - erf\frac{z}{\sqrt{4D_H t}}) \tag{3-3}$$

where c_0 is the concentration at the surface that is constant in time. During charging c_0 is assumed to be a constant.

Fick's second law can also be solved numerically. The evolution in the concentration profile due to a small time step Δt can be described as:

$$c(z,t+\Delta t) = c(z,t) + \frac{\partial c}{\partial t}\Delta t = c(z,t) + D_H\frac{\partial^2 c}{\partial z^2}\Delta t \tag{3-4}$$

This type of solution is used by commercial software such as DICTRA (Thermo-Calc Software 2012) according to the Euler forward method. By careful selection of time-steps Δt and using small distances, the concentration profile and its evolution with time can be solved.

3.2 Hydrogen solubility and diffusivity

Experimental data on the hydrogen solubility in ferritic iron is reviewed in Kiuchi and McLellan (1983). This solubility data (mole-fraction) has been fitted in this work according to Equation 3-5, and is also shown in Figure 3-1. The experimental results included in Figure 3-1 are for polycrystalline iron, which is relevant to the investigated material in the present study.

$$c_H = 0.00229 \cdot e^{(-\frac{28,584}{RT})} \tag{3-5}$$

The diffusion coefficient can be directly taken from the evaluation by Kiuchi and McLellan (1983), based on reported data in 20 different reports. The diffusion of hydrogen in ferrite is given as follows, in unit m^2/s:

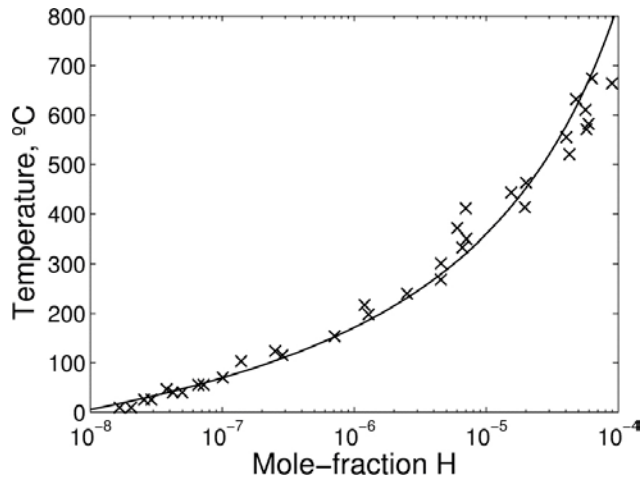$$D_H = 7.32 \cdot 10^{-8} \cdot e^{(-\frac{5,690}{RT})} \qquad\qquad (3\text{-}6)$$

Figure 3-1. *Experimentally determined hydrogen solubility according to Kiuchi and McLellan (1983), compared with fitted relation for hydrogen solubility according to (3-5).*

4 Materials and experiments

4.1 Material

The Swedish Nuclear Fuel and Waste Management Co (SKB) provided test material, which is a ferritic nodular cast iron, EN-GJS-400-15U in SS-EN 1563:2012. The chemical composition is given in Table 4-1 (Martinsson et al. 2010). Four blocks of nodular cast iron were received. They were cut out from a disc from the BWR insert with the SKB internal identity I55, see Figure 4-1. The thickness of the BWR disc was approximately 20 cm. X-ray analysis on the blanks confirmed that no large pores or inclusions (>1 mm) were present in the material.

Bulk hydrogen content for the as-received cast iron was 1.7 wtppm (Martinsson et al. 2009).

Table 4-1. The chemical composition of the investigated cast iron I55, wt% (Martinsson et al. 2010).

C	Si	Mn	S	P	Cr	Ni	Mg	Cu	C_{ekv}*	Fe
3.64	2.28	0.14	0.027	0.006	0.03	0.039	0.044	0.035	0.035	Bal

* $C_{ekv} = \%C + (\%Si/4) + (\%P/2)$.

4.2 Bar specimen for hydrogen charging

Bar specimens were taken from the BWR insert I55, see Figure 4-2. The dimension of the bar specimens is 7 mm in diameter and 65 and 85 mm in length, respectively. 65 mm bar specimens were used for hydrogen charging and degassing. 85 mm bars were used for hydrogen charging, degassing and microstructural examination. Surface of the bar specimens was finally polished using 400 dash emery paper. All the specimens were cleaned in water and ethanol and then dried with hot blow air to prevent from oxidising.
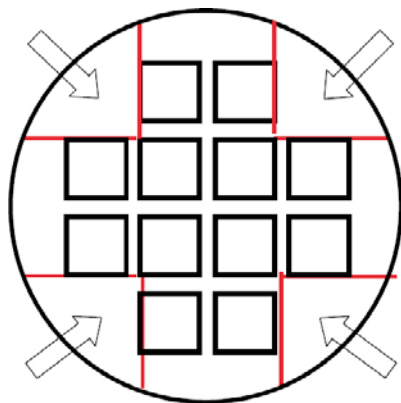

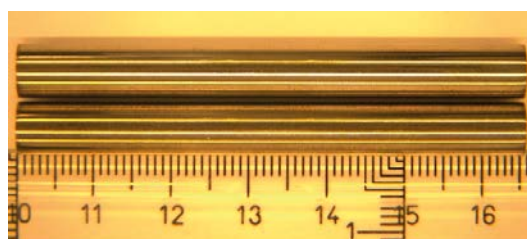*Figure 4-1. The disc from the BWR insert I55, after Martinsson et al. (2010).*

Figure 4-2. Bar specimen taken from the BWR insert I55 used for electrochemical hydrogen charging.

4.3 Electrochemical hydrogen charging, and degassing

Generally, by placing the charged object and the counter electrode in a beaker filled with an electrolyte and by applying a constant current density to create a difference in electrochemical potential between the charged object and the counter electrode, it is important to ensure the following reaction at the counter electrode to occur.

$$2H_2O \rightarrow O_2(g) + 4H^+ + 4e^- \tag{4-1}$$

where H^+ and e^- are released through decomposition of water. The rate of the process can be affected by the choice of electrolyte. The released components are then included in the following reactions taking place at the surface of the charged object:

$$2H^+ + 2e^- \rightarrow 2H_{ads} \tag{4-2}$$

$$2H_{ads} \rightarrow H_2(g) \tag{4-3}$$

$$H_{ads} \rightarrow H_{abs}. \tag{4-4}$$

The atomic hydrogen produced at the surface of the charged object will either form hydrogen gas or evaporate or will be absorbed into the bulk of the charged object. A more detailed description of electrochemical charging can be found in Martinsson et al. (2009).

A schematic illustration of electrochemical hydrogen charging setup and actual pictures taken in the present study are shown in Figure 4-3 and Figure 4-4, respectively. At the end of each cast iron specimen, a platinum wire was spot welded for electrical connection. A platinum mesh was used as counter electrode and the cast iron sample as a working electrode. The working and counter electrodes were connected to a DC regulated power supply (Model PS23023DL). A constant current density of 10 mA/cm^2 was applied between the working and the counter electrode. The working electrode was serving as a cathode and the counter electrode as an anode. The electrodes were immersed in an electrolyte containing 0.5 M Na_2SO_4 and 30 mg/l As_2O_3 where the arsenic compound acted as a hydrogen recombination inhibitor.

In the present study, all hydrogen charging experiments were carried out at room temperature. Time for hydrogen charging was chosen to 8, 16, 48 and 504 hours (the last corresponding to 3 weeks).

Degassing was conducted on hydrogen charged bar samples. The bar samples were firstly hydrogen charged for 504 hours. Then, the bar samples were exposed in air for one day at room temperature, for one week (168 hours) at room temperature, and for 624 hours (26 days) at 100°C, respectively.
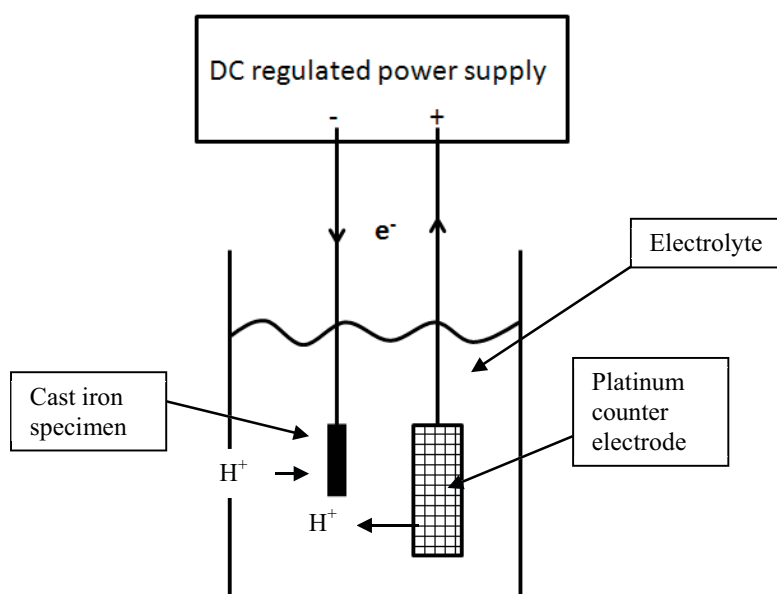

Figure 4-3. *Schematic illustration of electrochemical hydrogen charging setup. The cast iron specimen is used as a working electrode and the platinum mesh as a counter electrode.*
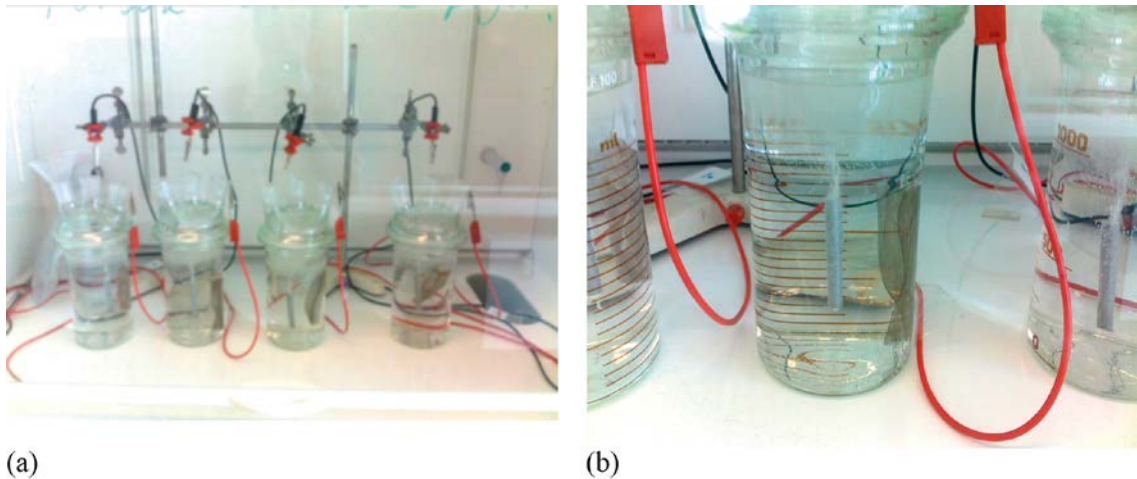
Figure 4-4. Pictures showing four cast iron specimens are electrochemically hydrogen charged in (a) and a close-up in (b).

4.4 Preparation of samples for hydrogen measurement

As soon as charging was completed, each 65 mm long charged bar was firstly lightly ground with 400 emery paper to remove any oxidization, and then divided into three equivalent parts, see parts A, B and C in Figure 4-5. The surface of part A had a ground surface. The two other parts B and C had the surface layer cut off by turning with different depths of 0.1/0.5 and 0.2/1 mm, respectively. Originally, 0.5 and 1 mm from surface were turned off for part B and C, respectively. It was soon realized that these turning depths were too large to quantify near subsurface hydrogen content. Hence, turning depths were reduced to 0.1 and 0.2 mm, respectively, for part B and C. After the part A, B and C had been turned into the right dimensions (diameters), they were further cut into two pieces (samples), each sample being 8 mm long. This means that there were two hydrogen measurements for each part. These samples were then kept in a small metal container, marked and finally stored in liquid nitrogen for hydrogen analysis.

The same procedure was applied for the 85 mm long charged bar specimens as well. Additionally, the 85 mm bar specimens were cut into an extra 15 mm long sample for microstructure analysis.

Commonly, it took less than 20 minutes to complete the above machining procedure from the stop of charging to storage in liquid nitrogen.
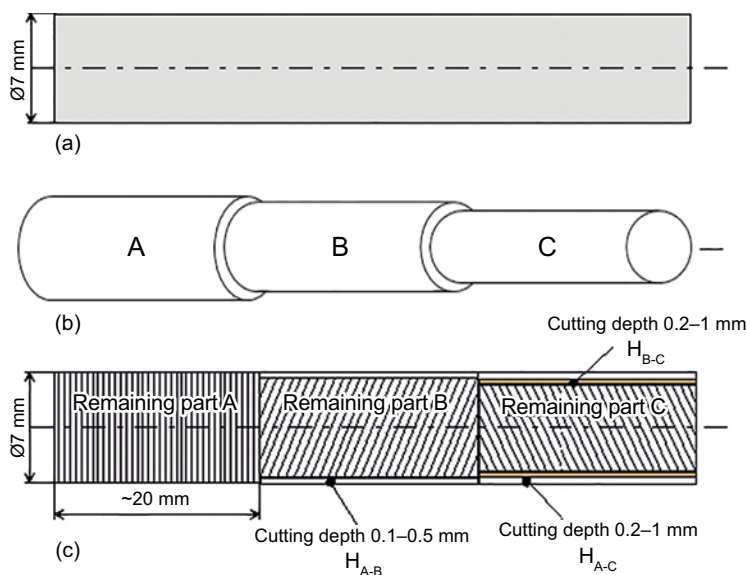

Figure 4-5. Hydrogen charged bar specimen for measurement of hydrogen content and for determination of hydrogen depth profile.

4.5   Measurement of hydrogen content

The analysis of hydrogen content was performed in a Leco Rhen 602 hydrogen determinator. Measuring method is the so-called melt extraction; the samples were melted in argon atmosphere whereupon the hydrogen in the sample was released in the form of gas. The hydrogen content is determined by measuring the heat conductivity of the gas mix during the analysis process.

4.6   Determination of hydrogen depth profile – method development

Prior to hydrogen measurement, volume and mass of each piece were carefully measured and recorded.

The hydrogen contents in the removed layers H_{A-B} and H_{A-C} were then calculated by comparing the hydrogen contents measured in the remaining parts A, B and C, respectively, within the same bar, see Figure 4-5. For instance, the hydrogen content in the removed layer H_{A-B} is determined as follow:

1) measure hydrogen contents in the remaining parts A and B,

2) calculate normalized iron mass (normalized to 8 mm in height) using measured volume and mass for remaining parts A and B,

3) calculate total numbers of hydrogen atoms in remaining parts A and B using related measured hydrogen content and normalized iron mass according to:

$$H = \frac{A \cdot M_H}{N_A \cdot m_{Fe}} \tag{4-5}$$

where H is the measured hydrogen content in wtppm, A the total numbers of hydrogen atoms, M_H the mass of hydrogen in g/mol, N_A the Avogadro constant $6.023 \cdot 10^{23}$ atom/mol and m_{Fe} normalized iron mass.

4) calculate total numbers of hydrogen atoms in the layer H_{A-B},

5) convert the total numbers of hydrogen atoms in H_{A-B} into the hydrogen content using (4-5). For clear and simple presentation of results, the half depth is chosen to represent the mean value of depth.

This procedure is also valid for calculation of the hydrogen content in the removed layer H_{A-C}. To obtain statistically representative results two to eight bars were tested at each set of parameters of charging and layer thickness.

4.7   Metallographic examination

Metallographic examinations were performed on the cross section of the degassed samples using the Leica DM IRM light optical microscope (LOM). The examinations were conducted several days after degassing. The samples were ground with successively finer grades of emery paper starting with 80 mesh and ending with 2,000 mesh. After grinding, the samples were mechanically polished using a polisher with polishing disk and diamond paste of different sizes down to 0.1 µm. The samples were etched in 2% Nital (2 ml HNO_3 and 100 ml Ethanol).

5 Results

5.1 Depth profile of charged hydrogen

Measured and calculated hydrogen contents after 8, 16, 48 and 504 hours charging are given in Table 5-1, Table 5-2, Table 5-3 and Table 5-4, respectively. The numbers of hydrogen charged bar samples are different for different charging times: 8, 4, 2 and 4 bar samples for charging time at 8, 16, 48 and 504 hours were employed, respectively. In the tables, the surface cutting depth for the corresponding remaining part, measured hydrogen content in the remaining part and the calculated hydrogen content in the removed layer are also shown, see Figure 4-5. The hydrogen content in the removed layer is calculated according to what is described in section 4.6.

Table 5-1. Measured and calculated hydrogen contents for 8 hours charging. Each value is a mean of two measurements.

Bar sample number	Remaining part	Surface cutting depth (mm)	Half cutting depth below surface (mm)	Measured H_2 in remaining part (wtppm)	Calculated H_2 in the removed layer (wtppm)
8_1	A	0		5.42*	
	B	0.06	0.03	4.685	58.68 (H_{A-B})
	C	0.185	0.0925	3.735	35.5 (H_{A-c})
8_2	A	0		5.77*	
	B	0.125	0.0625	3.125	129.86 (H_{A-B})
	C	0.195	0.0975	3.09	72.10 (H_{A-c})
8_3	A	0		3.595*	
	B	0.12	0.06	2.715	28.61 (H_{A-B})
	C	0.225	0.1125	2.665	17.75 (H_{A-c})
8_4	A	0		3.835*	
	B	0.105	0.0525	2.725	46.02 (H_{A-B})
	C	0.205	0.1025	2.89	20.39 (H_{A-c})
8_5	A	0		4.505*	
	B	0.475	0.2375	2.405	14.88 (H_{A-B})
	C	0.98	0.49	2.175	9.04 (H_{A-c})
8_6	A	0		3.735*	
	B	0.485	0.2425	2.430	9.84 (H_{A-B})
	C	0.99	0.495	2.21	6.57 (H_{A-c})
8_7	A	0		5.035*	
	B	0.105	0.0525	4.125	44.72 (H_{A-B})
	C	0.195	0.0975	3.345	33.93 (H_{A-c})
8_8	A	0		5.29*	
	B	0.08	0.04	3.21	114.77 (H_{A-B})
	C	0.175	0.0875	2.93	45.12 (H_{A-c})

* This value is used as hydrogen content in bulk material at corresponding depth of 1.75 mm (half of radius of the bar specimen).

Table 5-2. Measured and calculated hydrogen contents for 16 hours charging. Each value is a mean of two measurements.

Bar number	Remaining part	Surface cutting depth (mm)	Half cutting depth below surface (mm)	Measured H_2 in remaining part (wtppm)	Calculated H_2 in the removed layer (wtppm)
16_1	A	0		6.63*	
	B	0.125	0.0625	4.67	54.77 (H_{A-B})
	C	0.235	0.1175	4.76	32.14 (H_{A-c})
16_2	A	0		4.53*	
	B	0.095	0.0475	3.755	29.28 (H_{A-B})
	C	0.185	0.0925	4.065	12.70 (H_{A-c})
16_3	A	0		3.98*	
	B	0.14	0.07	3.405	17.05 (H_{A-B})
	C	0.25	0.125	2.75	20.22 (H_{A-c})
16_4	A	0		5.21*	
	B	0.135	0.0675	4.765	16.50 (H_{A-B})
	C	0.23	0.115	3.86	25.48 (H_{A-c})

* This value is used as hydrogen content in bulk material at corresponding depth of 1.75 mm (half of radius of the bar specimen).

Table 5-3. Measured and calculated hydrogen contents for 48 hours charging. Each value is a mean of two measurements.

Bar number	Remaining part	Surface cutting depth (mm)	Half cutting depth below surface (mm)	Measured H_2 in remaining part (wtppm)	Calculated H_2 in the removed layer (wtppm)
48_1	A	0		10.995*	
	B	0.5	0.25	8.44	20.26 (H_{A-B})
	C	1.025	0.5125	6.98	17.82 (H_{A-c})
48_2	A	0		9.085*	
	B	0.49	0.245	7.265	15.69 (H_{A-B})
	C	1.03	0.515	6.615	12.81 (H_{A-c})

* This value is used as hydrogen content in bulk material at corresponding depth of 1.75 mm (half of radius of the bar specimen).

Table 5-4. Measured and calculated hydrogen contents for 504 hours charging. Each value is a mean of two measurements.

Bar number	Remaining part	Surface cutting depth (mm)	Half cutting depth below surface (mm)	Measured H_2 in remaining part (wtppm)	Calculated H_2 in the removed layer (wtppm)
504_1	A	0		16.845*	
	B	0.49	0.245	11.335	43.63 (H_{A-B})
	C	0.99	0.495	10.0	29.92 (H_{A-c})
504_2	A	0		20.205*	
	B	0.53	0.265	19.33	23.99 (H_{A-B})
	C	1.02	0.51	21.53	17.79 (H_{A-c})
504_3	A	0		20.57*	
	B	0.49	0.245	13.795	52.74 (H_{A-B})
	C	0.99	0.495	14.175	32.59 (H_{A-c})
504_4	A	0		20.995*	
	B	0.515	0.2575	21.025	20.85 (H_{A-B})
	C	1.01	0.505	19.26	24.27 (H_{A-c})

* This value is used as hydrogen content in bulk material at corresponding depth of 1.75 mm (half of radius of the bar specimen).

Hydrogen content after 8, 16, 48 and 504 hours charging is given as a function of depth below the surface in Figure 5-1, Figure 5-2, Figure 5-3, Figure 5-4, respectively. Mean hydrogen content at given charging times as a function of depth below surface is shown in Figure 5-5. It is seen from these figures that

1) Hydrogen does diffuse into cast iron. If mean values are considered, hydrogen content can be higher than 50 wtppm adjacent to the surface compared to 1.7 wtppm for as-received bulk cast iron.

2) Hydrogen content decreases rapidly with increasing depth into the material.

3) Charging time has insignificant influence on hydrogen content adjacent to the surface, meaning that there might be a hydrogen saturation.

4) Charging time affects hydrogen content deep inside the material. The longer the charging time, the higher the hydrogen content. About 0.25 mm below the surface and deeper, the hydrogen content for longer charging times is twice as high as that for shorter charging times. For instance, at 1.75 mm below the surface, the hydrogen content is about 5 and 20 wtppm for 8 and 504 hour charging times, respectively, see Figure 5-5.
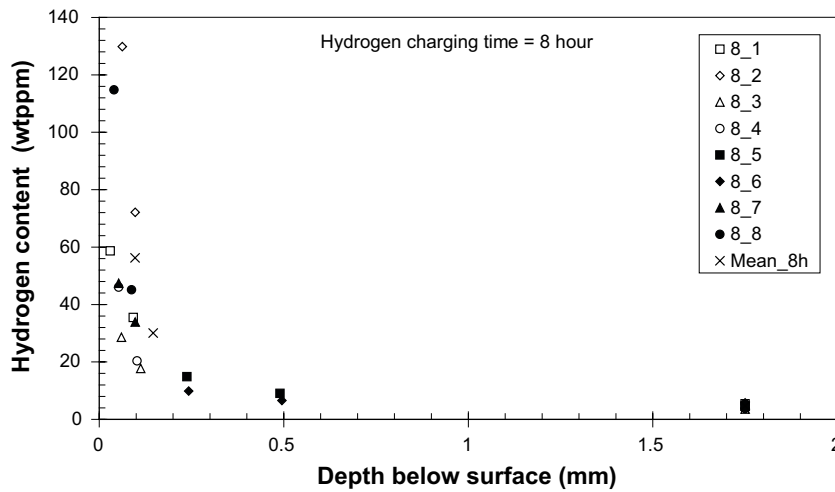
Figure 5-1. *Hydrogen content as a function of depth below surface for 8 hours charging time. Hydrogen content is measured and calculated on the eight bar samples.*
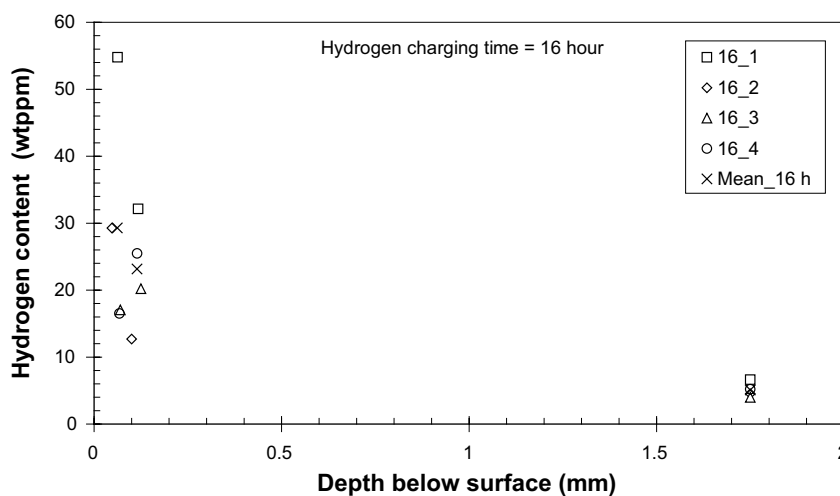
Figure 5-2. *Hydrogen content as a function of depth below surface for 16 hours charging time. Hydrogen content is measured and calculated on the four bar samples.*
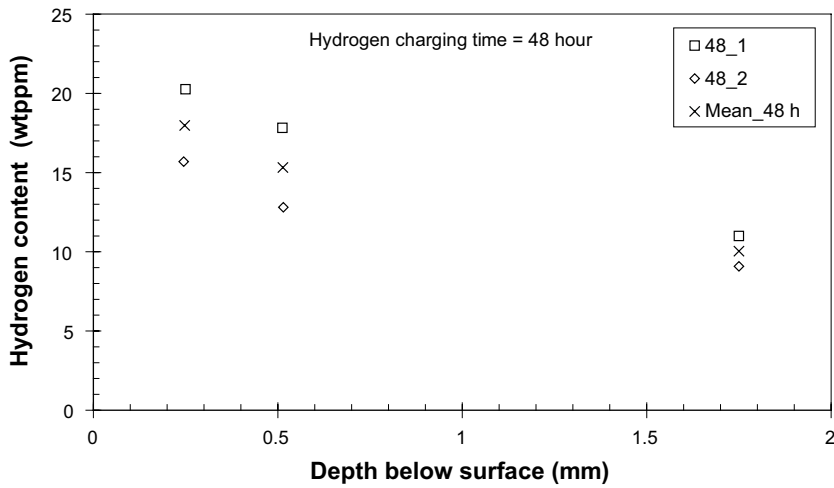
Figure 5-3. *Hydrogen content as a function of depth below surface for 48 hours charging time. Hydrogen content is measured and calculated on the two bar samples.*
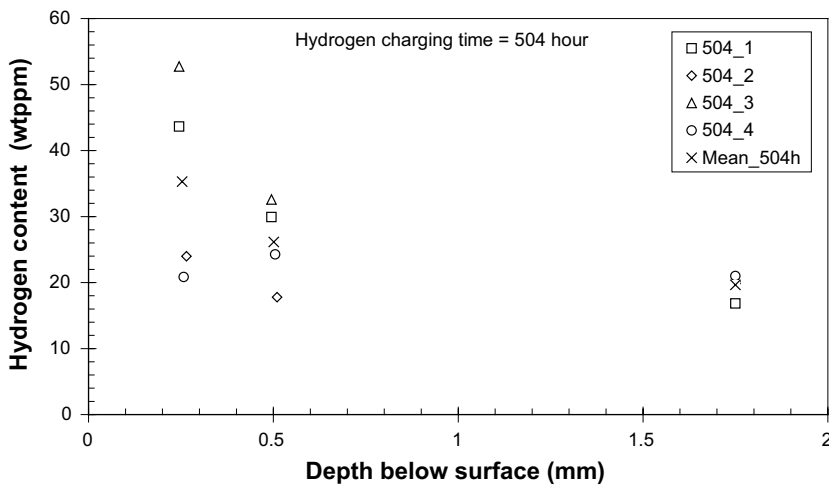
Figure 5-4. *Hydrogen content as a function of depth below surface for 504 hours charging time. Hydrogen content is measured and calculated on the four bar samples.*
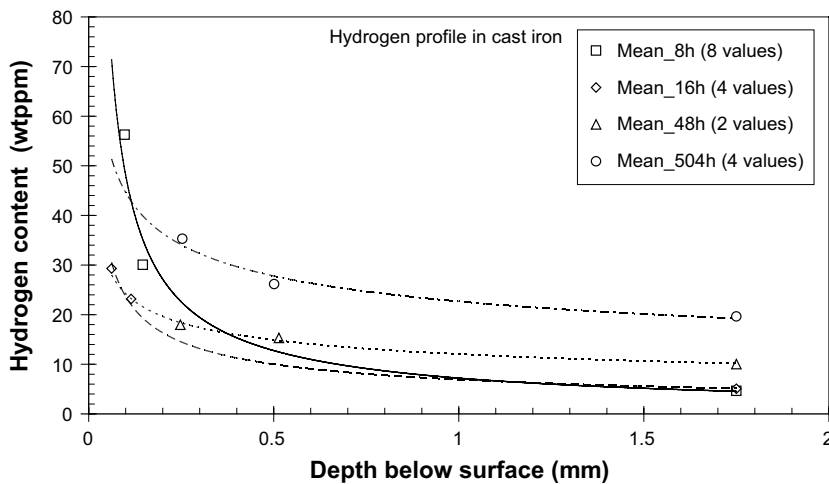
Figure 5-5. *Mean hydrogen content as a function of depth below surface for different charging times. Trend lines are included for clarification.*

5.2   Degassing

Degassing was conducted in air on the bar samples which had been hydrogen charged for 504 hours. After degassing, hydrogen content was measured and calculated in the same way as that for charged samples. The measured and calculated hydrogen contents degassed after 24 hours at room temperature, after 168 hours (1 week) at room temperature, and after 624 hours at 100°C are shown in Table 5-5. The hydrogen content at given degassing conditions as a function of depth below surface is exhibited in Figure 5-6, in which 504 hour hydrogen charging results without degassing are included for comparison. It is clear that

1) Hydrogen does diffuse out of cast iron.

2) The longer the degassing time and the higher the degassing temperature, the more the hydrogen escapes from the cast iron.

3) Hydrogen content decreases markedly at 100°C after 624 hours, i.e. from 35 to about 5 wtppm adjacent to the surface and from about 20 to 2.9 wtppm at 1.75 mm below the surface. Actually, these hydrogen contents are only slightly higher than that as-received bulk cast iron.

4) As a result of degassing, the highest hydrogen content may occur at subsurface. The hydrogen content at surface and deep inside the material is lower than that at subsurface, c.f. Figure 5-6 and Figure 5-5.

Table 5-5. **Measured and calculated hydrogen contents for degassed bar sample. Only one bar sample was used at each given degassing condition. Each value is a mean of two measurements.**

Degassing condition	Remaining part	Surface cutting depth (mm)	Half cutting depth below surface (mm)	Measured H_2 in remaining part (wtppm)	Calculated H_2 in the removed layer (wtppm)
24 hours at RT	A	0		15.465*	
	B	0.2	0.10	14.485	31.57 (H_{A-B})
	C	0.28	0.14	14.64	24.95 (H_{A-c})
168 hours at RT	A	0		14.96*	
	B	0.53	0.265	14.76	20.76 (H_{A-B})
	C	1.02	0.51	14.46	23.65 (H_{A-c})
624 hours at 100°C	A	0		2.9*	
	B	0.49	0.245	3.065	1.49 (H_{A-B})
	C	0.99	0.495	2.57	5.16 (H_{A-c})

* This value is used as hydrogen content in bulk material at corresponding depth of 1.75 mm (half of radius of the bar specimen).
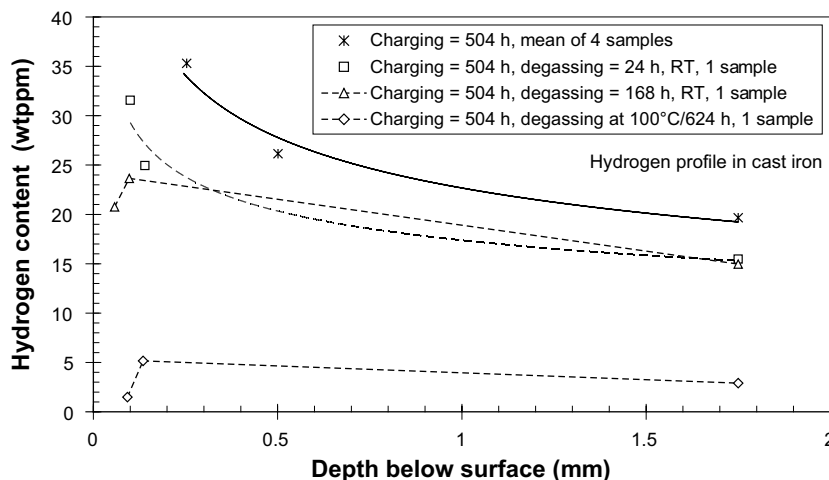
Figure 5-6. *Hydrogen content as a function of depth below surface at given degassing conditions. All the samples were firstly hydrogen charged to 504 hours (3 weeks). RT refers to room temperature. The 504 hour hydrogen charging results without degassing are included for comparison.*

5.3 Metallographic examination

Metallographic examinations were carried out on both as-received and degassed samples. The as-received cast iron consists of ferrite, few pearlite and nodular graphite, see Figure 5-7. Pores are also observed. Microstructure for degassed samples is given in Figure 5-8, Figure 5-9 and Figure 5-10 for different degassing condition, respectively. It is difficult to see observable difference in microstructure between the as-received and the degassed materials, verified also by another investigation, see Swerea Swecast (2012).
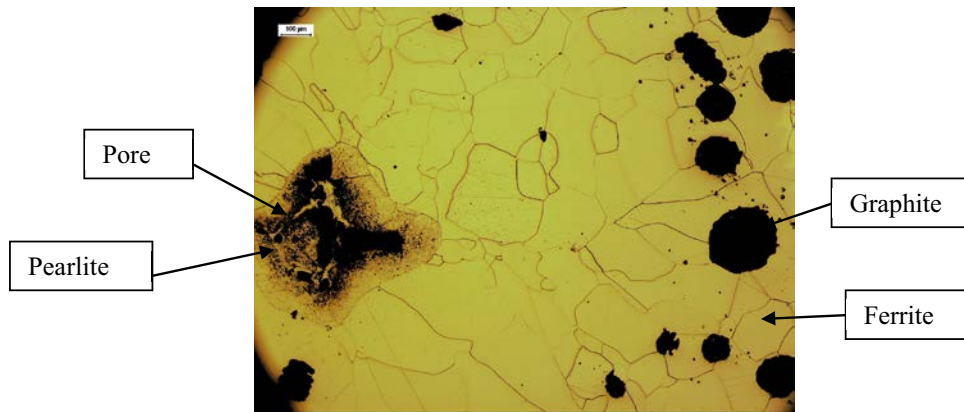
Figure 5-7. LOM image showing the as-received cast iron consisting of ferrite, pearlite and nodular graphite. Pores are also observed.
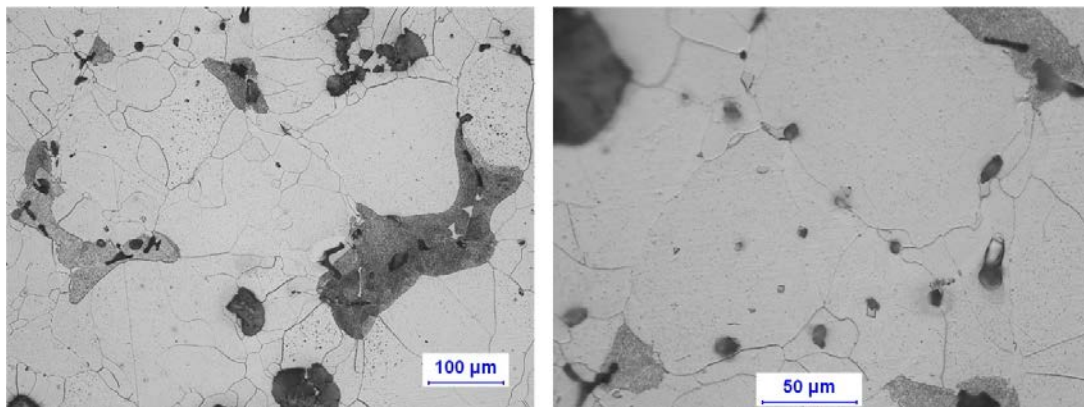
Figure 5-8. LOM images showing degassed sample after 24 hours at room temperature. Ferrite, pearlite, nodular graphite and pores are observed.
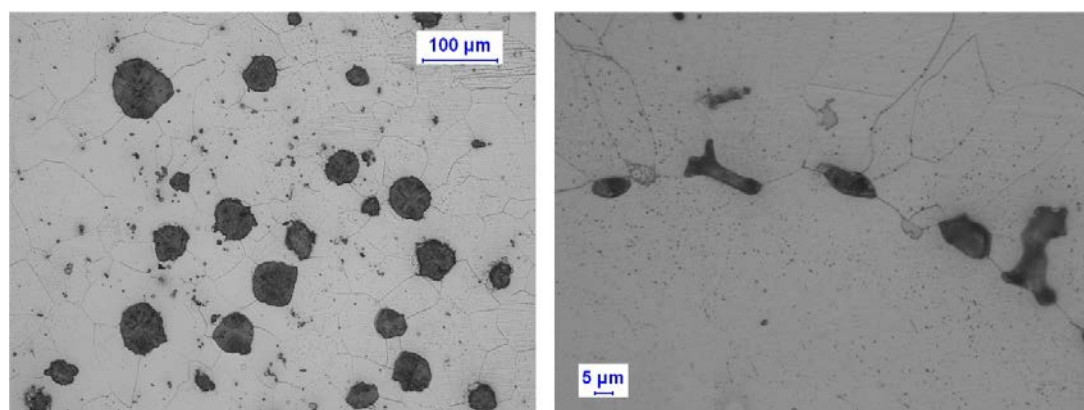
Figure 5-9. LOM images showing degassed sample after 168 hours at room temperature. Ferrite, pearlite, nodular graphite and pores are observed.
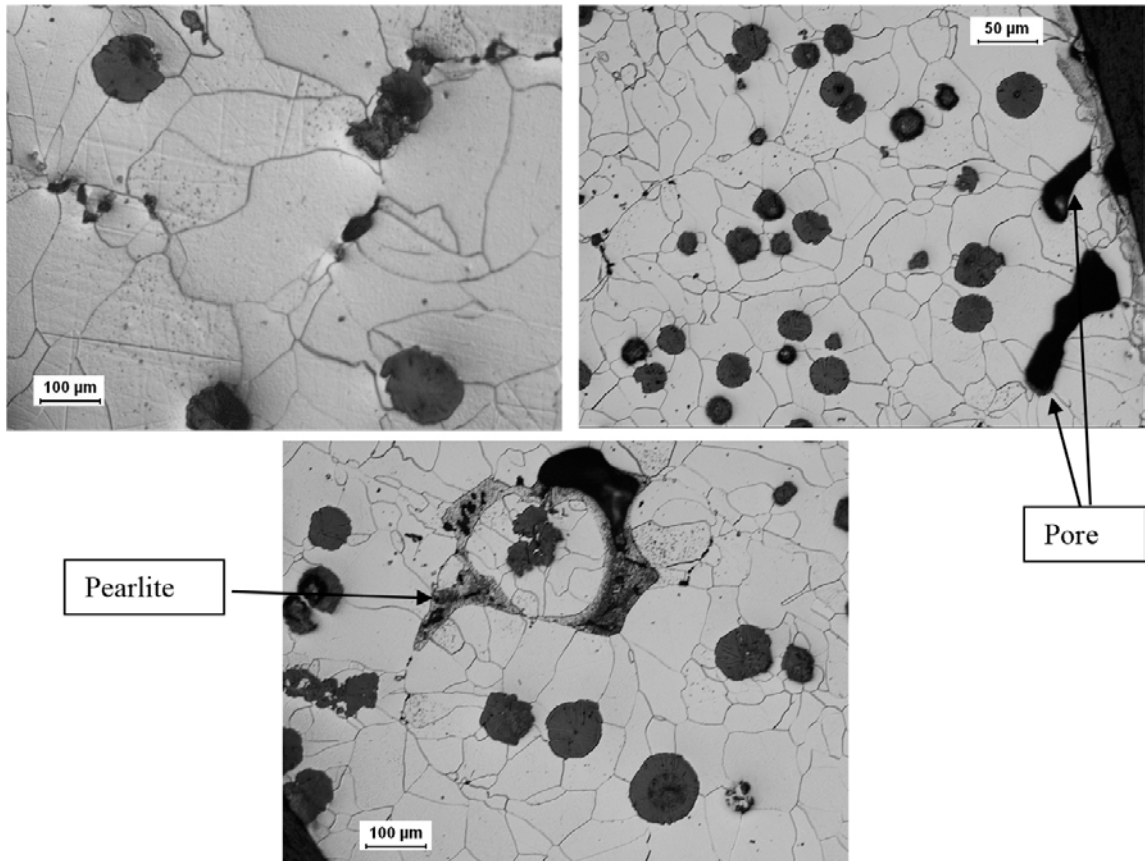
Figure 5-10. LOM images showing degassed sample after 624 hours at 100°C. Ferrite, pearlite, nodular graphite and pores are observed.

5.4 Modelling of hydrogen solubility and diffusivity

5.4.1 Analytical approach

The analytical approach gives the following expression for the concentration profile as function of time and distance.

$$c(z,t) = 40 \text{ wtppm } (1 - erf \frac{z}{\sqrt{4D_H t}}) \tag{5-1}$$

40 wtppm has been chosen as the hydrogen solubility at surface, based on the measurements made in this work. The value for the diffusion coefficient D_H is taken from (3-6). Simulations using (5-1) at 8, 16, 48, and 504 charging hours are shown in Figure 5-11. It can be seen that the simulated hydrogen transport in iron is much faster than the experimentally determined hydrogen profile. The diffusion distance is about two orders of magnitudes larger than that experimentally determined. For these simulations the measured hydrogen contents in iron are assumed to be the solubility values.

By making the following assumptions, hydrogen diffusion in iron can be modelled with much better accuracy:

- Hydrogen transport in the matrix is based on the solubility of hydrogen in ferrite, as described by Equation (3-5).

- The high measured hydrogen contents from the charged samples are due to crystal defects in lattice (dislocations, porosity, grain boundaries etc).

- The supply of hydrogen to these defects will be made through hydrogen transport in solid solution.
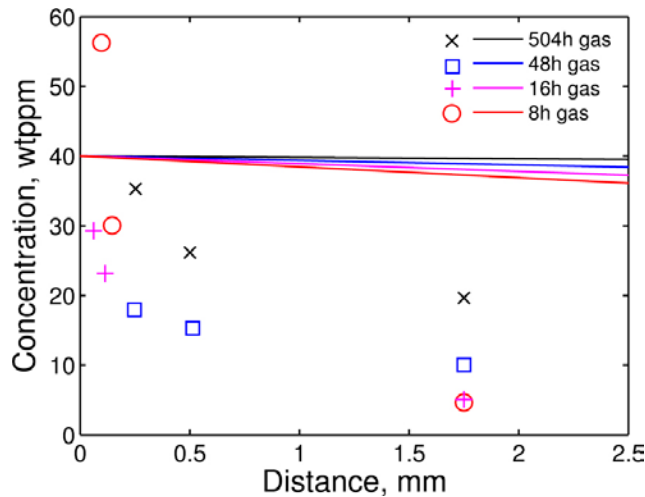
Figure 5-11. *Hydrogen content (lines) according to (5-1) assuming all measured hydrogen is in solution. The different times corresponds to different charging times. Measured and calculated hydrogen contents from Figure 5-5 (symbols) are included for comparison.*

If hydrogen is diffusing in low concentrations and supplies many crystalline defects with hydrogen, it will result in slower average hydrogen transport. The amount of defects can be estimated from the measured hydrogen content in the as-received material, compared with the theoretical hydrogen solubility in iron, i.e. 1.7 and 0.0004 wtppm, respectively. This gives 4,200 times higher measured value compared to the solid solution value. Assuming that the average hydrogen transport takes place 4,200 times slower due to all these crystalline defects, modified hydrogen diffusion can be written as:

$$c(z,t) = 40\ wtppm\,(1 - erf\,\frac{z}{\sqrt{4D_H t\,/4,200}})$$

(5-2)

By using this expression the measured hydrogen content can be better described, as shown in Figure 5-12.
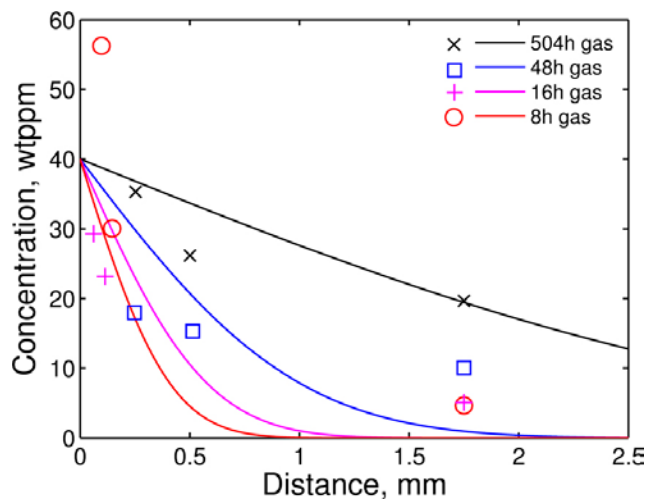
Figure 5-12. *Hydrogen content (lines) according to (5-2) assuming only hydrogen in solid solution determines the rate of hydrogen flux. Measured and calculated hydrogen contents from Figure 5-5 (symbols) are included for comparison. The different times indicate different charging times.*

5.4.2 Numerical approach

The simulated hydrogen charging using the numerical approach, (3-4), is shown in Figure 5-13. The results are similar to the analytical solution, c.f. Figure 5-12. The longer charging times give longer diffusion distances.

Hydrogen degassing is simulated for 24 and 168 hours at room temperature and 624 hours at 100°C, respectively. The results are presented in Figure 5-14. Simulations are based on the charged profile given in Figure 5-5 for 504 hours, which is also shown in Figure 5-14 for comparison. The condition of degassing used for the simulation is that the boundary for hydrogen concentration is held at 1.7 wtppm (as-received material). Due to a low concentration of hydrogen at the surface, an outward flux of hydrogen out of the material will take place. In addition, some hydrogen also diffuses in inward direction to level off any gradients in hydrogen. The general trend found in the experimental data can be understood through these simulations, with longer times or higher temperature for degassing giving lower concentrations. However, the measured hydrogen contents close to the surface of room-temperature samples are quite high. This is not in agreement with simulations, and one explanation is that the simulations assume an ideal transport from the material to the atmosphere. In real conditions there can be an interface effect that slows down the loss of hydrogen.

Another simulation is made using the assumption that no hydrogen is allowed to escape out of the material, and all hydrogen can only diffuse inside the material. The boundary condition on the outermost point of the simulation is therefore no hydrogen flux outwards but only inwards. The results are shown in Figure 5-15. It can be seen that the simulated values at 24 hours and 168 hours at room temperature are all higher than the experiments, indicating a redistribution of hydrogen concentration.
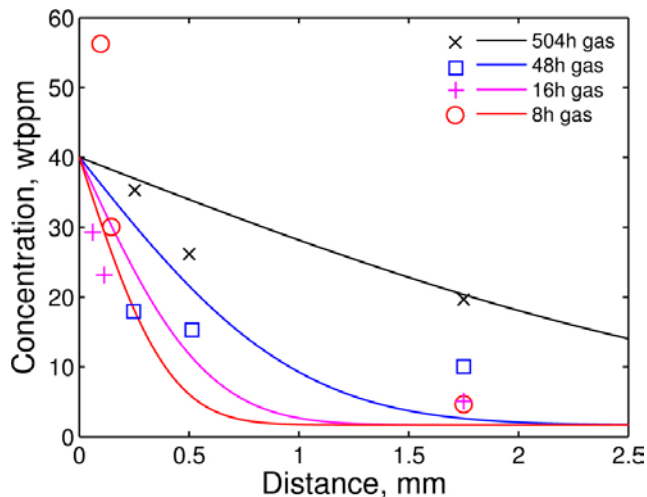
Figure 5-13. *Simulated hydrogen content (lines) according to (3-4). Measured and calculated hydrogen contents from Figure 5-5 (symbols) are included for comparison.*
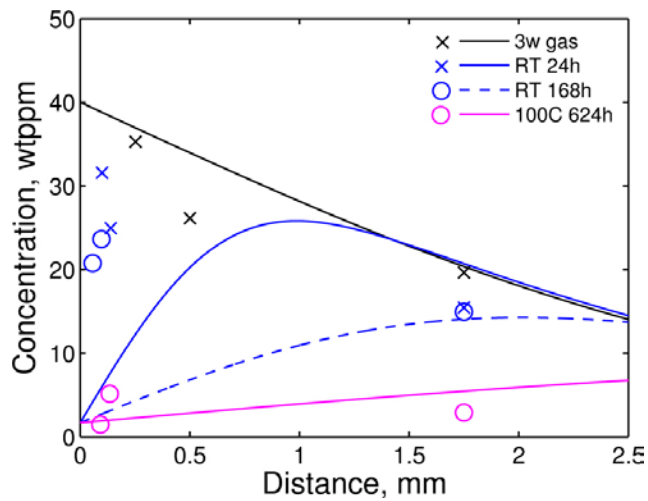
Figure 5-14. *Simulated hydrogen degassing profile (colour lines) at room temperature for 24 and 168 hours, and at 100°C for 624 hours. The initial concentration profile (black line) and measured and calculated hydrogen contents from Figure 5-5 (symbols) are included for comparison.*
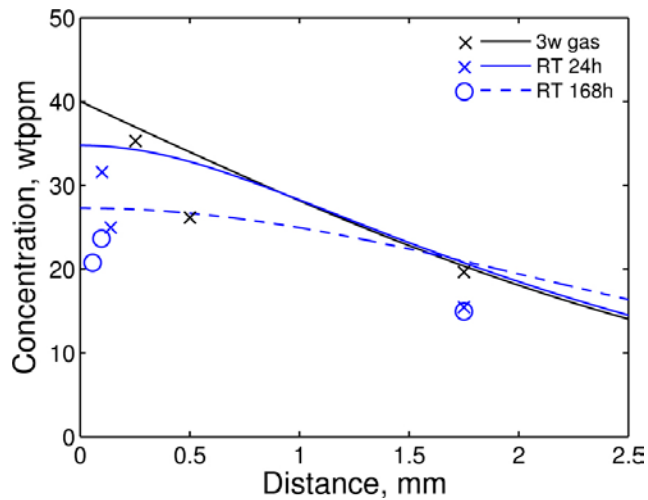

Figure 5-15. *Simulated hydrogen degassing profile for 24 and 168 hours at room temperature (colour lines). No hydrogen is allowed to escape out of material. Measured and calculated hydrogen contents from Figure 5-5 (symbols) are included for comparison.*

6   Discussion

Two main methods have been established to charge hydrogen into a metallic material; namely 1) thermal (Nakahara and Okinaka 1988, Pan and Byrne 1985) and 2) electrochemical charging (Nakahara and Okinaka 1988, Dull and Raymond 1974, Panagopoulos and Zacharopoulos 1994). The driving force for the thermal charging is hydrogen pressure gradient. This method is a traditional approach and requires high temperature and high hydrogen pressure and usually takes long time. One drawback associated with the thermal charging is grain growth and the grain growth rate increases with increasing temperature. Grain growth by thermal charging has been reported in Martinsson et al. (2009). In addition, reproducibility of the thermal charging to get desired hydrogen content is poor (Martinsson et al. 2009).

The driving force for electrochemical charging is the difference of potential between anode and cathode. There are advantages for this charging method. It offers convenient means for injecting atomic hydrogen into material at ambient temperature. Grain size is kept unaffected. It can build up higher levels of hydrogen in a relative short period. Cathodic protection will prevent corrosion attack on the charged object. Besides, this method has been proven in Martinsson et al. (2009) for the same material as used in the present case. All these reasons determine the choice of electrochemical charging in the present study.

It should be mentioned that the conditions used in the present electrochemical charging, namely a constant current density of 10 mA/cm^2 and use of As_2O_3, may generate defects on and /or below surface. A study using scanning electron microscope (Pérez Escobar et al. 2011) showed the formation of surface hydrogen blisters and hydrogen induced cracks in a pure iron and a ferrite-bainite steel after electrochemical hydrogen charging. The cracks were formed more easily in pure iron, corresponding to the faster blister formation. They found also that blister formation was influenced by the sample surface roughness.

Methods for preparation of sample for hydrogen measurement and for determination of hydrogen depth profile have been originally developed and used in a previous study for copper (Martinsson and Sandström 2012). These methods have been further developed in the present study. Although this method is rough concerning depth variation and can be refined, it gives quantitative values of the hydrogen content at related depth and clear profile of hydrogen in relation to depth. Both are important to understand hydrogen diffusion and distribution. Actually, the accuracy of hydrogen measurement are to a large extent determined by control of charging process, degree of degassing, and precise measurements of bulk hydrogen content and corresponding mass.

Hydrogen does diffuse into cast iron. This is apparent from Figure 5-1 to Figure 5-4. It is natural that the highest hydrogen content appears at outer surface, where the hydrogen content can be several ten times higher than that for the as-received material. Charging time plays a minor role in hydrogen content at the outer surface. Even after 8 hours, the hydrogen content can be as high as 130 wtppm (the highest value for all tested charging times in the present study). Higher hydrogen content than 130 wtppm has not obtained, even though charging times have been in fact prolonged to 504 hours. This indicates that there might be a hydrogen saturation at the outer surface.

There is a saturation of hydrogen concentration at the outer surface after a short charging time of 8 hours, see Figure 5-5. The surface saturation of hydrogen concentration might be related to defects which are very strong trap sites for hydrogen. The saturation of hydrogen concentration has been reported in ferrous alloys (Farrel 1970). The saturation time and hydrogen concentration depend on the charging conditions (electrolyte, charging current and temperature), type of steel and sample geometry (Dong et al. 2009). A continuous change of hydrogen concentration at subsurface and throughout bulk sample is observed, see also Figure 5-5. The longer the charging time, the higher the hydrogen content deeper inside the cast iron. At 1.75 mm below the surface, the hydrogen contents are 4.65 wtppm after 8 hour and 19.65 wtppm after 504 hour, respective.

Hydrogen content decreases rapidly with increasing depth into the cast iron, see Figure 5-5. This trend follows a power law. The power law trend of hydrogen distribution in terms of depth has been observed in a similar study of hydrogen charging of Cu-OFP (Martinsson and Sandström 2012),

which states that electrochemical charging of Cu-OFP bulk samples strongly increases the hydrogen content in the surface layer and the penetration depth is about 50 μm. The study (Martinsson and Sandström 2012) also shows that the hydrogen content in the bulk is unaffected although the charging time as long as 504 hours has been used. This is not the case for the cast iron in the present study, in which the hydrogen content charged after 504 hours is 19.65 wtppm at 1.75 mm below the outer surface. This value is more than one order of magnitude higher than 1.7 wtppm measured in the as-received bulk cast iron.

The power law behaviour of hydrogen distribution in terms of depth, see Figure 5-5, can be simply described as:

$$H = \alpha \cdot D^\beta \tag{6-1}$$

where H is the measured hydrogen content in wtppm, D the depth in mm, α and power β are experimentally determined constant. The values of α and β are shown in Table 6-1. It can be seen that the coefficient α and power β take larger values at longer charging time. Caution must be taken to extrapolate outside the fitting range by using equation 6-1.

Scatters of hydrogen content are observed at the same charging time for different samples, see Figure 5-1 to Figure 5-4. The scatters are more distinct adjacent to surface. Causes for the scatter are thought to be measuring errors, which in turn affect the calculation results, and local microstructural variation. In the present case, routine like preparation of samples and method for measurements has been established to minimise discrepancy caused by measurement. Furthermore, the cast iron consists of ferrite, few pearlite, pore and graphite, see Figure 5-7. Pore and graphite may act as entrapment sites binding hydrogen atoms and resulting in locally higher hydrogen content.

The work trying to quantitatively correlate pore and hydrogen content has been made elsewhere, see Swerea Swecast (2012), on the charged and degassed samples given in Table 5-5, including the as-received cast iron for comparison. In Swerea Swecast (2012) 1 the porosity is measured adjacent to the outer surface (1 mm in depth) as well as at the inner area of the samples (~3 mm below the outer surface) using SEM. The results show that amount of porosity is similar between different samples and between surface and inner area. Therefore, the work concludes that hydrogen charging does not affect size or amount of porosity in the cast iron, although locally high porosity associated with defect is sometimes found.

Influence of hydrogen on mechanical properties of cast iron has been reported in Martinsson et al. (2009) and in Matsuno et al. (2012). Apparently, both tensile and creep properties were lowered due to the presence of hydrogen, i.e. tensile ductility reduced by nearly 50% (Martinsson et al. 2009). The hydrogen content reported in Martinsson et al. (2009) can be compared with that measured in the present case. For example, immediately after charging the creep specimens contain 10 wtppm hydrogen (bulk values) (Martinsson et al. 2009). Comparing to the present study, this value is higher than shorter times charging (8 and 16 hours) by a factor of approximately 2, similar to that for 48 hours, and lower than that for 504 hours by a factor up to 2.

It is observed that hydrogen content has been reduced from 10 to 3.4 wtppm after 4 weeks of creep testing at room temperature (Martinsson et al. 2009). This indicates hydrogen degassing with time. Hydrogen degassing does occur in the present study as well, see Table 5-5 and Figure 5-6. The longer the degassing time and the higher the degassing temperature, the more the hydrogen escapes from the cast iron. After one week at room temperature, hydrogen content has reduced from 20 to 15 wtppm deep inside the cast iron (bulk value). After 624 hours at 100°C, hydrogen content has lowered to 2.9 wtppm, which is comparable to that for the as-received material (1.7 wtppm).

Table 6-1. Values of constants α and β in (6-1) for given charging times.

Charging time	α	β
8 hours	7.21	−0.824
16 hours	6.092	−0.533
48 hours	12.06	−0.303
504 hours	22.68	−0.294

As a result of degassing, the highest hydrogen content may occur at subsurface, especially at longer time and higher temperature, see Figure 5-6. The change of the highest hydrogen content from surface to subsurface is natural and is a consequence of redistribution of hydrogen by diffusing either into atmosphere or deeper into the cast iron. This behavior is also verified by the simulations, see Figure 5-15.

Not only increased hydrogen content affects detrimentally tensile and creep properties but also porosity could act as crack initiation site and influence mechanical properties. Quantitative measurements of porosity on the fracture surface of tensile tested specimens made of the cast iron having SKB internal identity I57 show that area fraction of pore and dross varies between 16–31%, see Appendix.

The theoretical solubility of hydrogen in iron is much lower than the measured content of hydrogen. Nevertheless, the theoretical solubility of hydrogen in ferrite can be adopted in order to simulate the hydrogen transport during charging. When using the measured hydrogen content in diffusion simulations, the hydrogen transport is overestimated by about two orders of magnitude. On the other hand, based on the assumption that only a part of the present hydrogen takes part in the transportation, the concentration profiles at charging could be reproduced.

Hydrogen degassing in air shows agreement to simulations, with the expected time/temperature behaviour, see Figure 5-15. But, the measured hydrogen content close to the surface is much higher than predicted when using a low boundary content of hydrogen, see Figure 5-14. If the hydrogen content at the surface is low enough, there should be a quite rapid degassing close to the surface. However, this is not verified by the experiments. This could be due to difficulties in degassing iron in an oxygen atmosphere at low temperature. In addition, the assumption of a rapid charging with hydrogen quickly distributing in all defects does not necessarily imply an equally rapid degassing. For instance, if hydrogen during charging reacts with internal entrapments it will become trapped and the degassing will then be difficult. In fact, it is demonstrated in this work that the assumption of limited hydrogen leaving the surface seems a good assumption for room temperature samples.

7 Conclusions

Using an electrochemical charging method, hydrogen has been charged into nodular cast iron originally containing 1.7 wtppm hydrogen (SKB internal identity I55) at times up to 504 hours at room temperature. Hydrogen is degassed at room temperature and at 100°C at times up to 624 hours. Methods for sample preparation and for measurement and calculation of hydrogen content have been further developed and used to describe the hydrogen profile in relation to depth. Hydrogen diffusion and degassing have been simulated. The following conclusions can be drawn:

1. Hydrogen does diffuse into the cast iron. The highest calculated hydrogen content of 130 wtppm appears at the outer surface.

2. Hydrogen content decreases rapidly with increasing depth into the material. This trend fits a power law in the fitting range.

3. Hydrogen content at the surface approaches saturation after only a short charging time of 8 hours. Further increase in time does not increase the surface hydrogen content. Instead, the hydrogen diffuses deep into the cast iron and the hydrogen content for longer charging times can be 4 times as high as that for shorter charging times at 1.75 mm below the surface.

4. Hydrogen does diffuse out of the cast iron. The longer the degassing time and the higher the degassing temperature, the more the hydrogen escapes from the cast iron. At 100°C after 624 hours, hydrogen content decreases from 35 to 5 wtppm adjacent to the surface and from 20 to 2.9 wtppm at 1.75 mm below the surface.

5. As a result of degassing, the highest hydrogen content may occur at subsurface. The hydrogen contents at the outer surface and deep inside the cast iron are lower than that at subsurface.

6. No clear correlation between amount of porosity and hydrogen content is found. Hydrogen entrapment sites and hydrogen-induced surface blisters/cracking are not identified yet. More studies are needed.

7. The diffusion equations can be used to estimate the hydrogen charging and degassing behaviour. The hydrogen profile in relation to depth has been simulated and described.

8. The thermodynamic data (solubility data) is decisive to model the hydrogen transport into cast iron. Based on the fact that the measured hydrogen content is several orders of magnitude higher than the theoretical solubility values, the assumption that only hydrogen in solid solution controls the hydrogen transport has to be adopted.

Acknowledgements

References

SKB's (Svensk Kärnbränslehantering AB) publications can be found at www.skb.se/publications.
References to SKB's unpublished documents are listed separately at the end of the reference list.
Unpublished documents will be submitted upon request to document@skb.se.

Dayal R K, Parvathavarthini N, 2003. Hydrogen embrittlement in power plant steels. Sādhanā 28, 431–451.

Dong C F, Liu Z Y, Li X G, Cheng Y F, 2009. Effects of hydrogen-charging on the susceptibility of X100 pipeline steel to hydrogen-induced cracking. International Journal of Hydrogen Energy 34, 9879–9884.

Dull D L, Raymond L, 1974. Electrochemical techniques. In Raymond L (ed). Hydrogen embrittlement testing. Philadelphia: American Society for Testing and Materials. (ASTM Special Technical Publication 543), 20–33.

Farrel K, 1970. Cathodic hydrogen absorption and secere embrittlement in a high strength steel. Corrosion 26, 105–110.

Kiuchi K, McLellan R B, 1983. The solubility and diffusivity of hydrogen in well-annealed and deformed iron. Acta Metallurgica 31, 961–984.

Martinsson Å, Sandström R, 2012. Hydrogen depth profile in phosphorus-doped, oxygen-free copper after cathodic charging. Journal of Materials Science 47, 6768–6776.

Martinsson Å, Wu R, Sandström R, 2009. Influence of hydrogen on mechanical properties of nodular cast iron. KIMAB-2009-118, Swerea KIMAB AB, Sweden.

Martinsson Å, Andersson-Östling H C M, Seitisleam F, Wu R, Sandström R, 2010. Creep testing of nodular iron at ambient and elevated temperatures. SKB R-10-64, Svensk Kärnbränslehantering AB.

Matsuno K, Matsunaga H, Endo M, Yanase K, 2012. Effect of hydrogen on uniaxial tensile behaviour of a ductile cast iron. International Journal of Modern Physics: Conference Series 6, 407–412.

Nakahara S, Okinaka Y, 1988. The hydrogen effect in copper. Materials Science and Engineering A 101, 227–230.

Pan Y, Byrne J G, 1985. Thermal charging effects of hydrogen in copper and Cu-A alloys. Materials Science and Engineering, 215–223.

Panagopoulos C N, Zacharopoulos N, 1994. Cathodic hydrogen charging and mechanical properties of copper. Journal of Materials Science 29, 3843–3846.

Pérez Escobar D, Miñambres C, Duprez L, Verbeken K, Verhaege M, 2011. Internal and surface damage of multiphase steels and pure iron after electrochemical hydrogen charging. Corrosion Science 53, 3166–3176.

Raiko H, 2005. Disposal canister for spent nuclear fuel – design report. Posiva 2005-02, Posiva Oy, Finland.

SKB, 2009. Design premises for a KBS-3V repository based on results from the safety assessment SR-Can and some subsequent analyses. SKB TR-09-22, Svensk Kärnbränslehantering AB.

SKB, 2010. RD&D Programme 2010, Programme for research, development and demonstration of methods for the management and disposal of nuclear waste. SKB TR-10-63, Svensk Kärnbränslehantering AB.

SS-EN 1563:2012. Founding – Spheroidal graphite cast irons. Stockholm: Swedish Standards Institute.

Thermo-Calc Software, 2012. DICTRA, version 26 (build 2532). Stockholm: Thermo-Calc Software AB.

Wanhill R J H , Barter S A , Lynch S P, Gerrard D R, 2011. Prevention of hydrogen embrittlement in high strength steels, with emphasis on reconditioned aircraft components. In Corrosion fatigue and environmentally assisted cracking in aging military vehicles. NATO Science and Technology Organization. Available at: http://ftp.rta.nato.int/public/PubFullText/RTO/AG/RTO-AG-AVT-140///
AG-AVT-140-20.pdf

Unpublished documents

Swerea SWECAST, 2012. Investigation report (Examination No 20429 issue 3). Swerea SWECAST. SKBdoc 1339593 ver 2.0, Svensk Kärnbränslehantering AB.

swerea|SWECAST

ISO
9001
SFK

INVESTIGATION REPORT

Date	Sample arrived	Order Company
2013-02-14	2012-01-21	Svensk Kärnbränslehantering AB
Examination No		Box 925
20524		572 29 OSKARSHAMN
Order No		Your Reference
9919		Sören Claesson

Assignment

Hydrogen charging was carried out on three nodular iron specimens taken from the insert I55. Different charging and degassing periods were used. The specimens marking and the corresponding charging and degassing data are presented below:

Sample	Charging time	Degassing time
A2	3 weeks	1 day
A3	3 weeks	1 week
A4	3 weeks	624 hour at 100°C
REF	-	-

In this work a quantitative analysis of the micro-porosity will be performed in order to reveal any possible influence of the H_2 charging on the size of the measured micro-porosity.

Implementation

All specimens were investigated with scanning electron microscope (SEM).

Previous investigation has shown that the hydrogen charging increases the material concentration of hydrogen in the area close to surface (from the sample surface, up to 1 mm inside the sample). In the present work the micro-porosity is measured in the outer (1 mm in depth) as well as at the inner area of the samples. Figures 2, 8, 14 and 19 show the investigated regions in the different sample.

The method for measuring the micro-porosity area is presented in report 20429.

Results

Figures 4-23 presents all of the detected micro-porosity from the outer as well as from the inner area of the samples.

The percentage of micro-porosity is presented in Table 1 for every sample and for each investigated region. Figure 1 illustrates the micro-porosity that measured on the area close to the sample surface accompanied with the micro-porosity measurements at the inner area of the samples.

swerea|SWECAST

Discussion
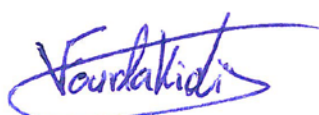
As can be seen in Figure 1 the amount of micro-porosity is similar in the inner and outer zone of A2 and A3 samples while in both samples the micro-porosity percent is lower than the percentage of micro-porosity in the Reference sample.

Sample A4 has a very high amount of micro-porosity that is concentrated at the outer region of the sample. This concentration cannot be attributed to the H_2 charging due to the fact that the percentage of micro-porosity in A2 and A3 samples is very low, although all the samples were induced in H_2 charging for the same time period. It is believed that the defects in A4 sample are formed during the solidification and coincidently appeared in the specific area.

Conclusions

The investigation results indicate that the H_2 charging does not affect the size or the amount of the micro-porosity in the samples. The high level of micro-porosity, at the outer area of A4 sample, is considered as coincidently appeared defect in the specific area.

Swerea SWECAST AB
Metallurgy and Materials Technology

Vasilios Fourlakidis

Reviewed: Lennart Sibeck

Table 1.Percentage of micro-porosity in the samples.

Sample	Micro-porosity (outer area), %	Micro-porosity (inner area), %
A2	0,016	0,015
A3	0,009	0,0091
A4	0,34	0,029
REF	0,025	0,036
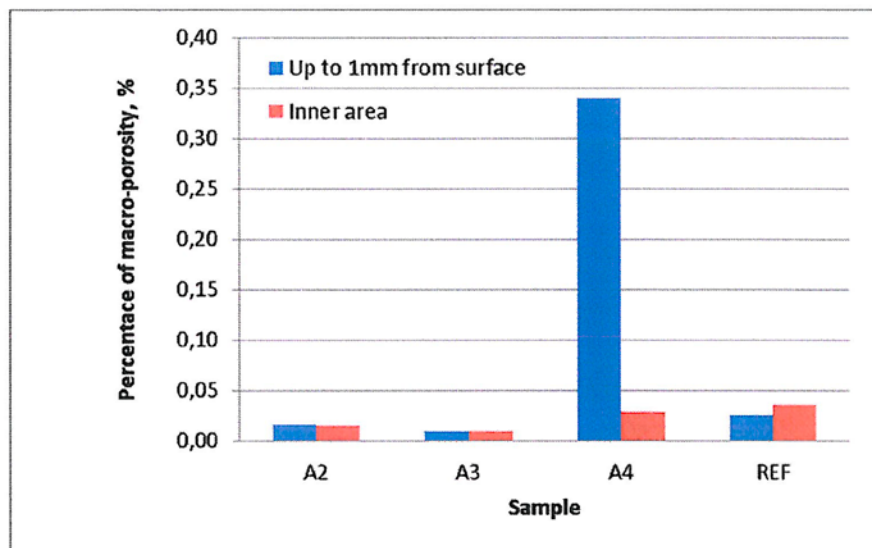
Figure 1. Percentage of micro-porosity in the outer area as well as in the inner area of the samples.
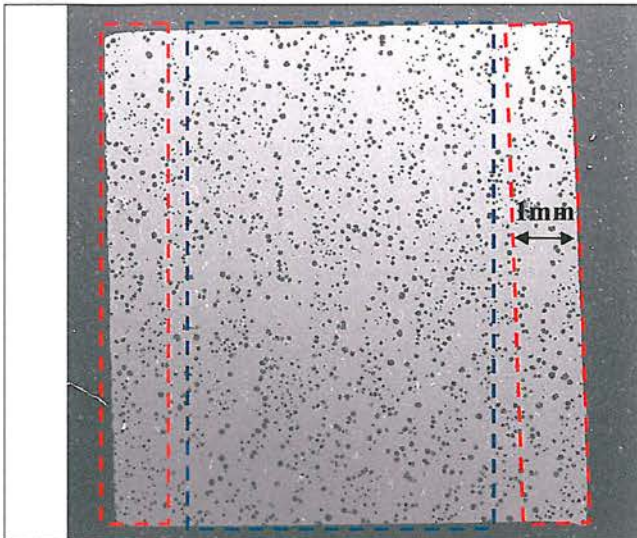
Figure 2.

Sample A2.

The red dashed lines indicate the outer area (up to 1 mm from the sample surface). The blue dashed lines show the inner investigated area.
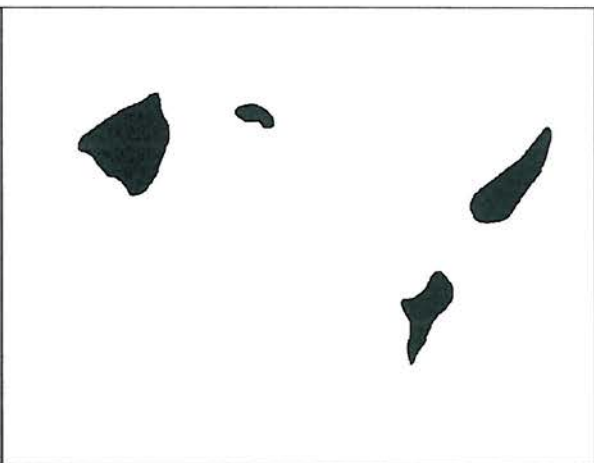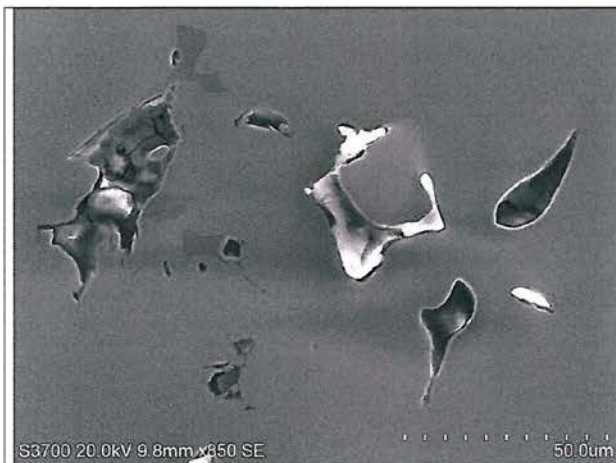
Figure 3. Sample A2, outer area. Micro-porosity (left) and the marked porosity used for image analysis (right).
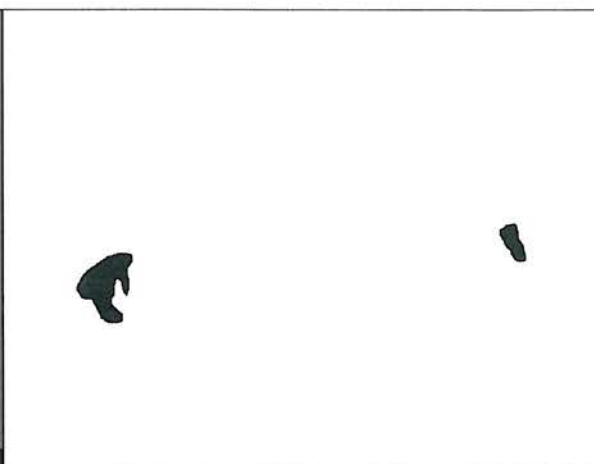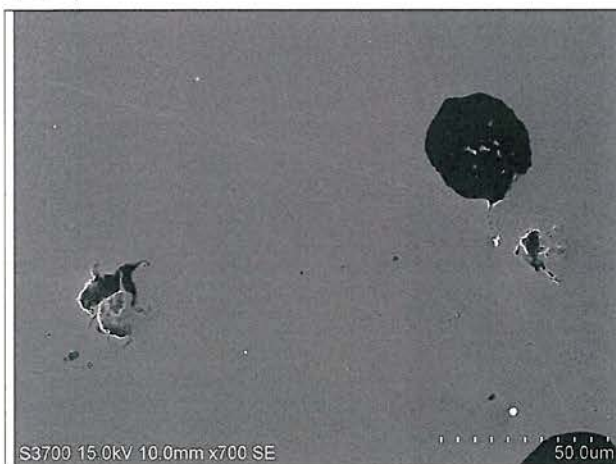
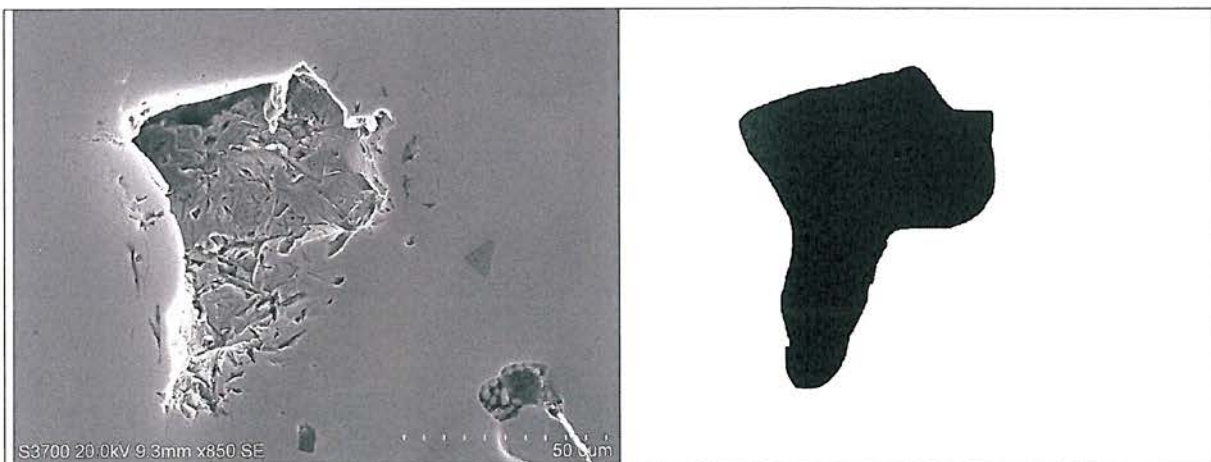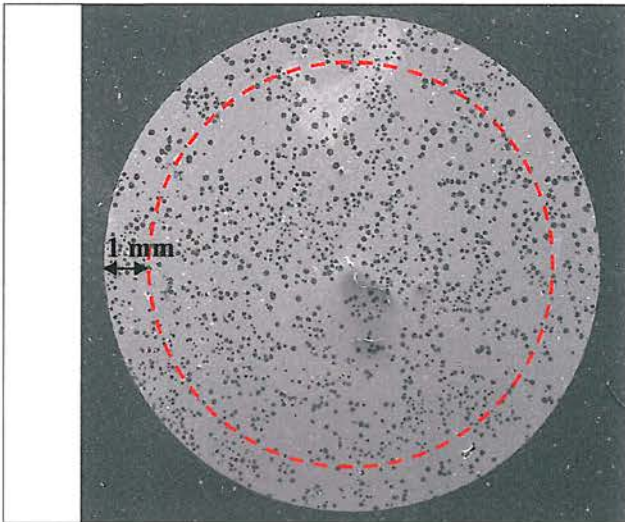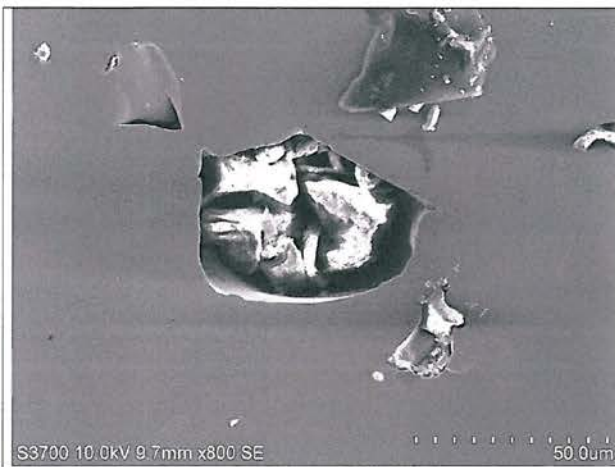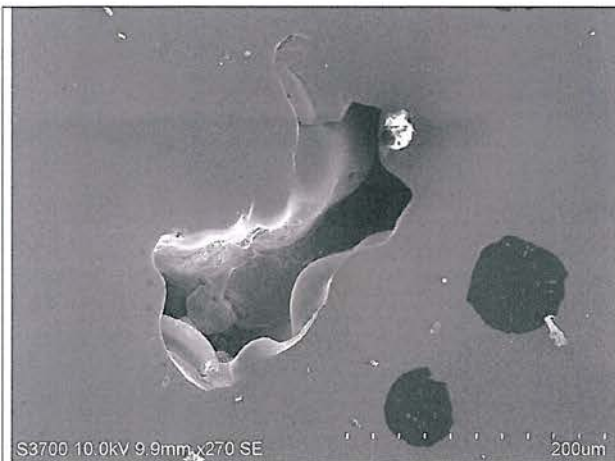Figure 4. Sample A2, outer area. Micro-porosity (left) and the marked porosity used for image analysis (right).
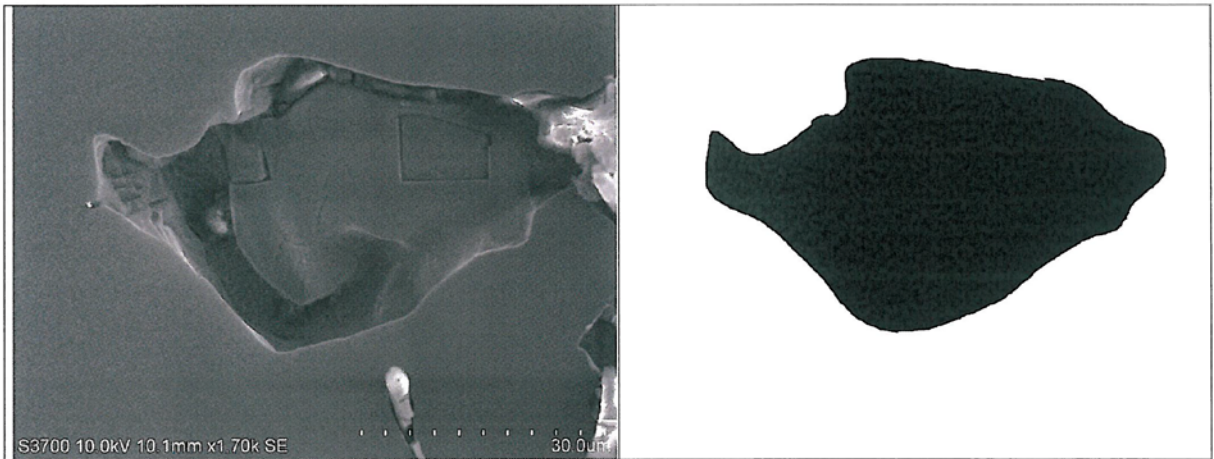
Figure 5. Sample A2, outer area. Micro-porosity (left) and the marked porosity used for image analysis (right).
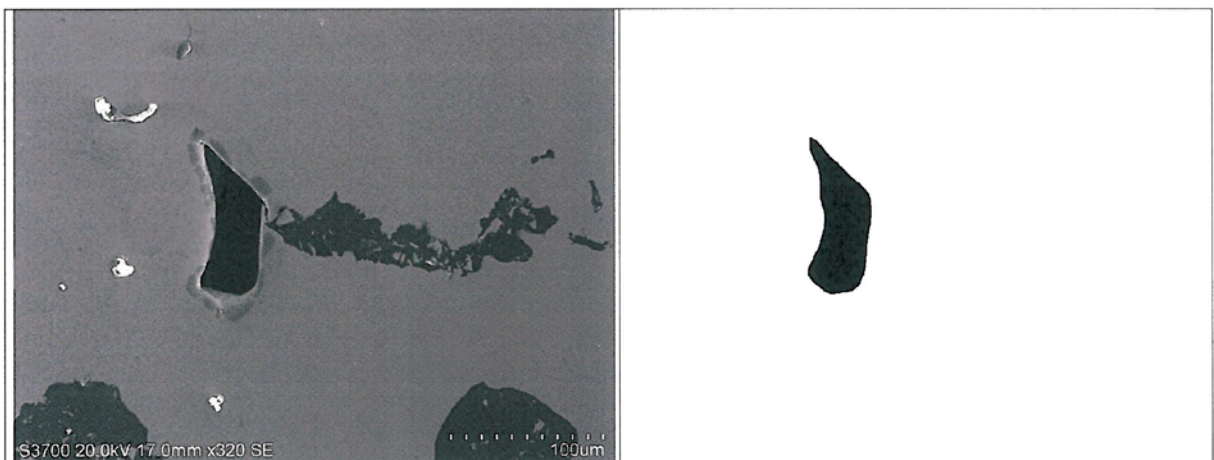
Figure 6. Sample A2, inner area. Micro-porosity (left) and the marked porosity used for image analysis (right).
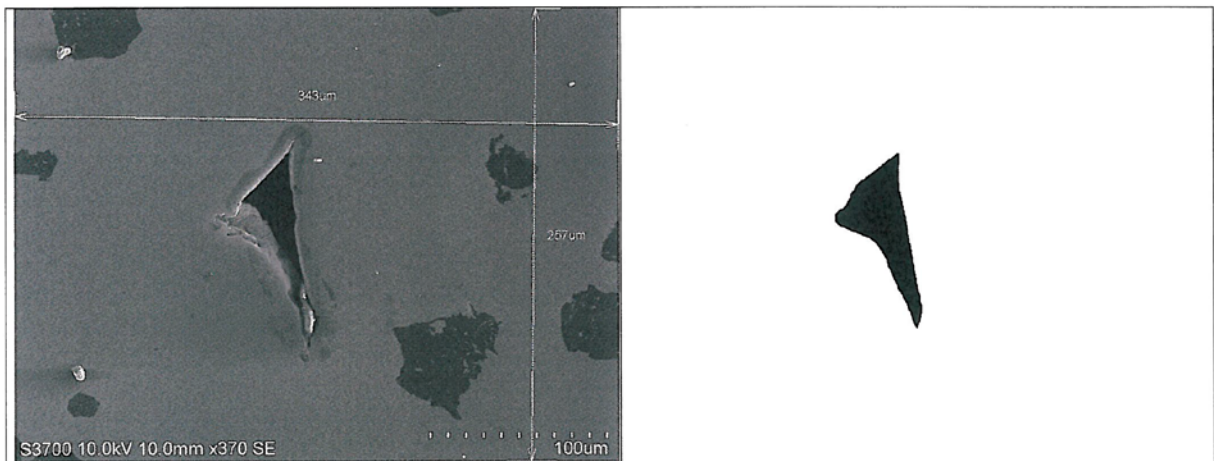
Figure 7. Sample A2, inner area. Micro-porosity (left) and the marked porosity used for image analysis (right).
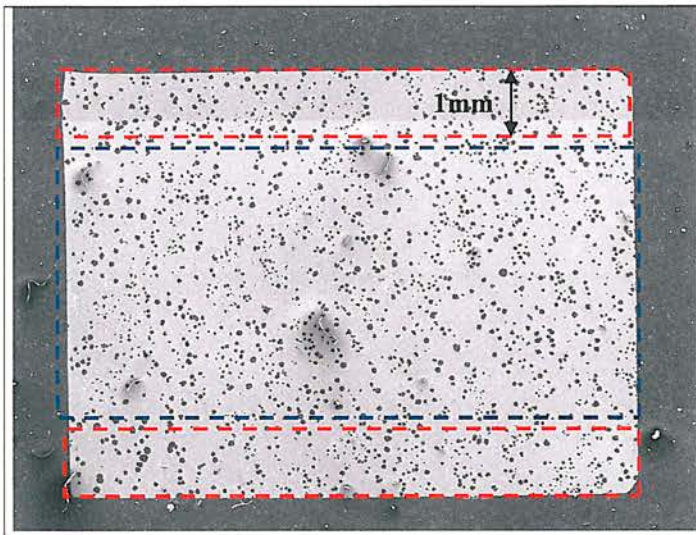
Figure 8.

Sample A3.

The red dashed lines indicate the outer area (up to 1 mm from the sample surface). The blue dashed lines show the inner investigated area.
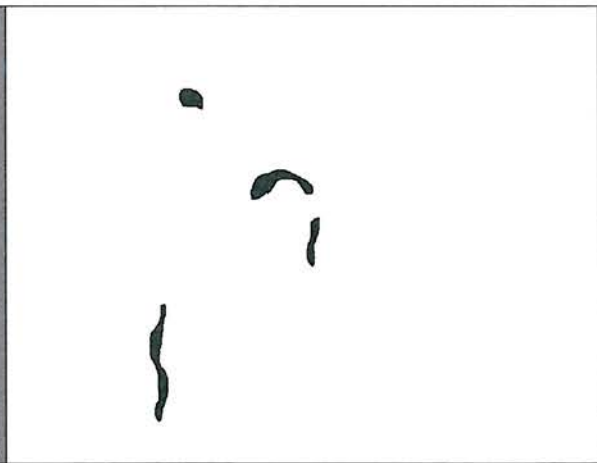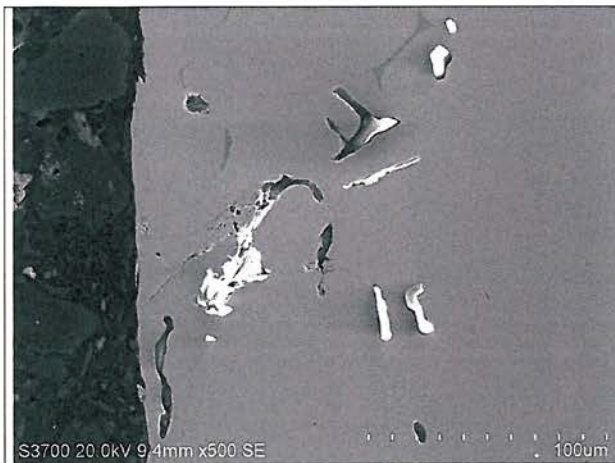
Figure 9. Sample A3, outer area. Micro-porosity (left) and the marked porosity used for image analysis (right).
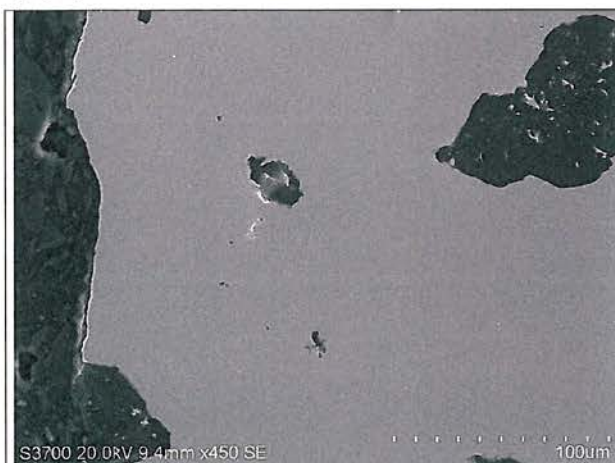
Figure 10. Sample A3, outer area. Micro-porosity (left) and the marked porosity used for image analysis (right).
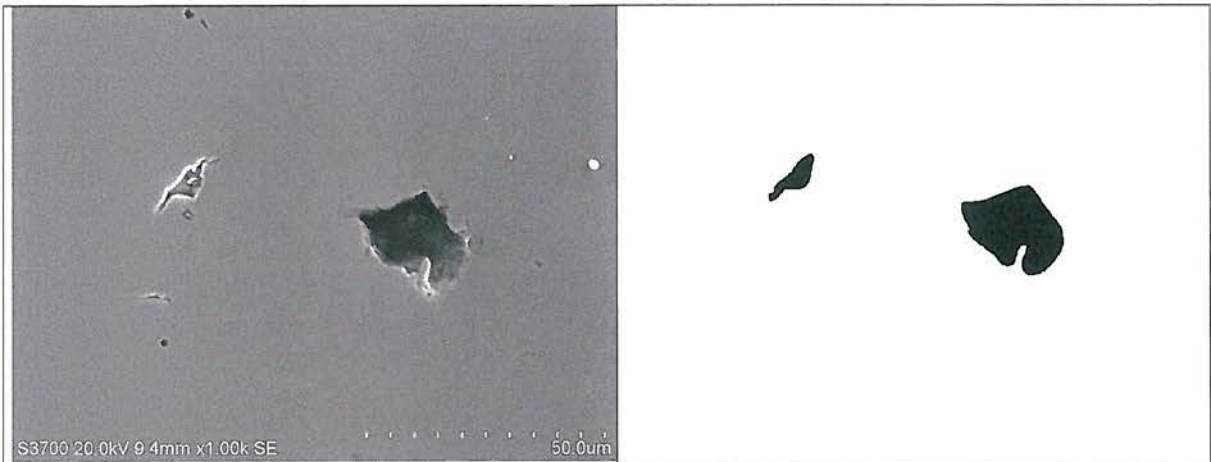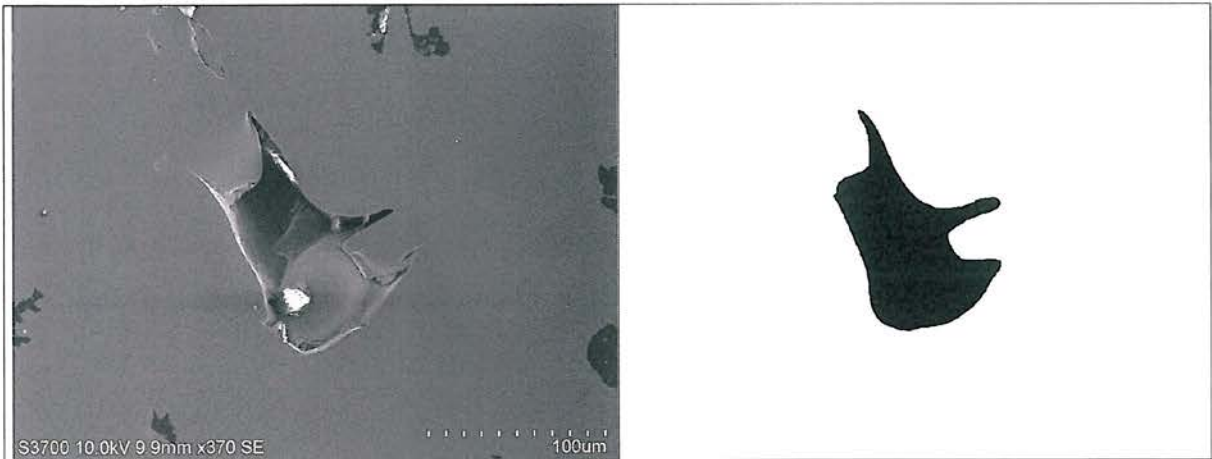
Figure 11. Sample A3, outer area. Micro-porosity (left) and the marked porosity used for image analysis (right).
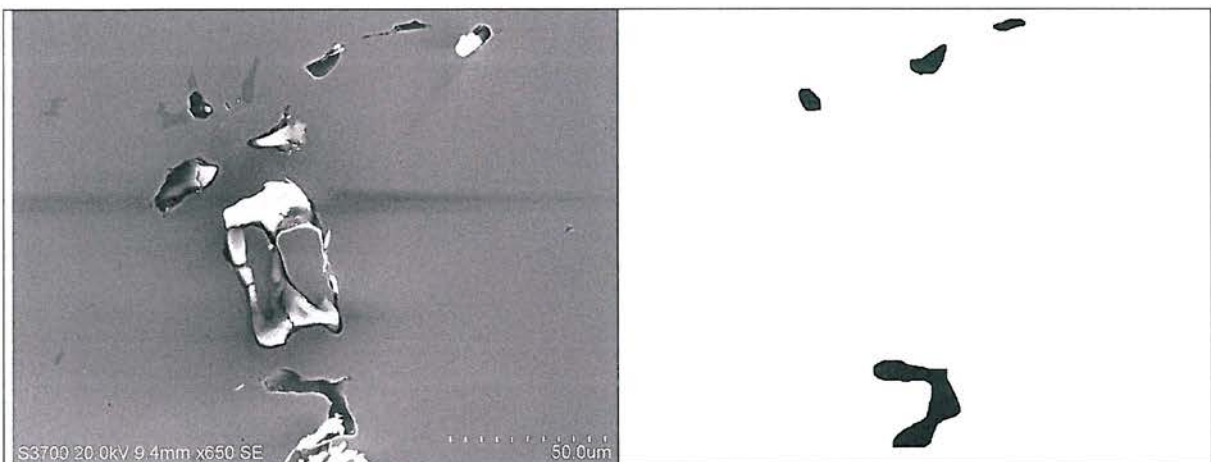
Figure 12. Sample A3, outer area. Micro-porosity (left) and the marked porosity used for image analysis (right).
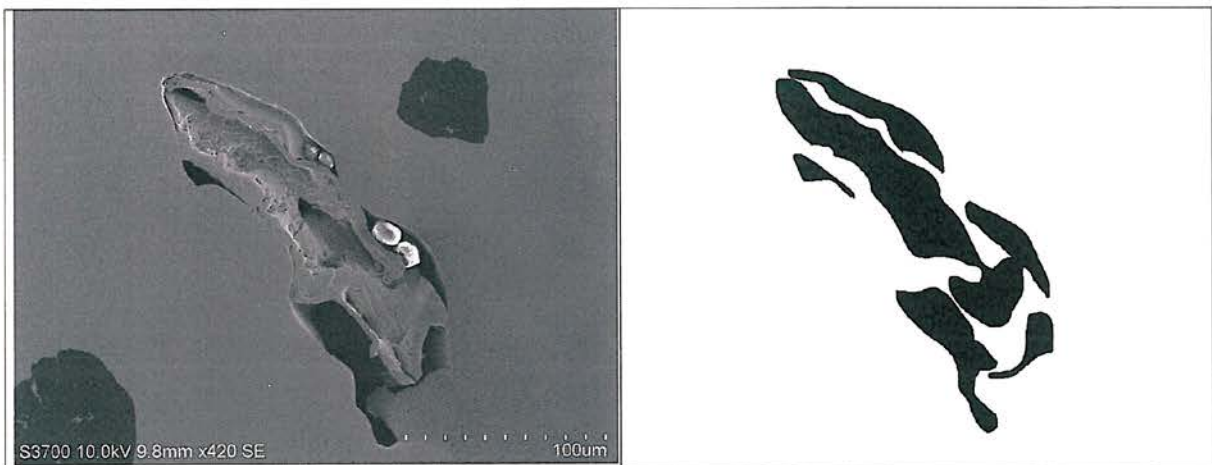

Figure 13. Sample A3, inner area. Micro-porosity (left) and the marked porosity used for image analysis (right).
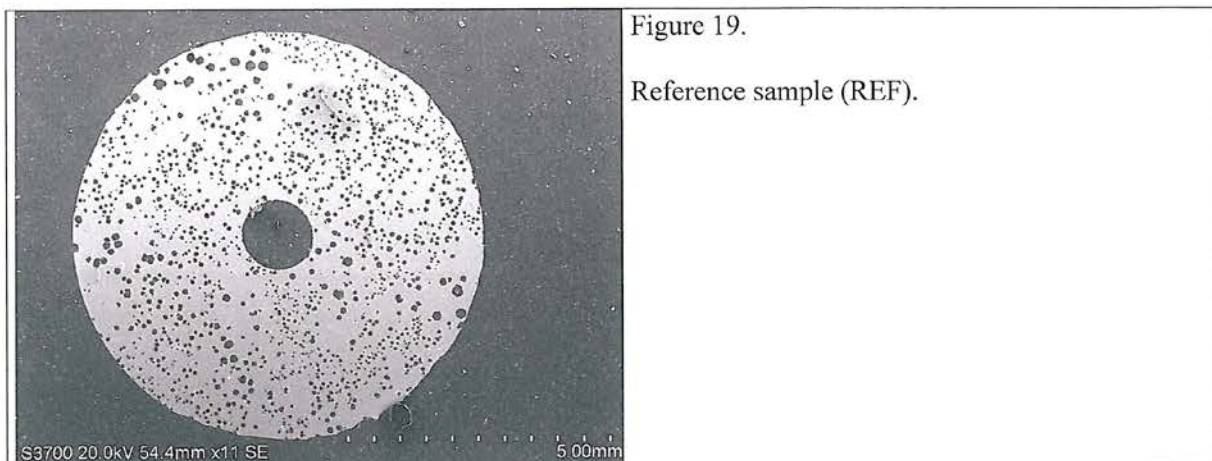
Figure 14.

Sample A4.

The dashed line indicates the division of the investigated areas.

Figure 15. Sample A4, outer area. Micro-porosity (left) and the marked porosity used for image analysis (right).

Figure 16. Sample A4, outer area. Micro-porosity (left) and the marked porosity used for image analysis (right).

Figure 17. Sample A4, outer area. Micro-porosity (left) and the marked porosity used for image analysis (right).

Figure 18. Sample A4, inner area. Micro-porosity (left) and the marked porosity used for image analysis (right).

Figure 19.
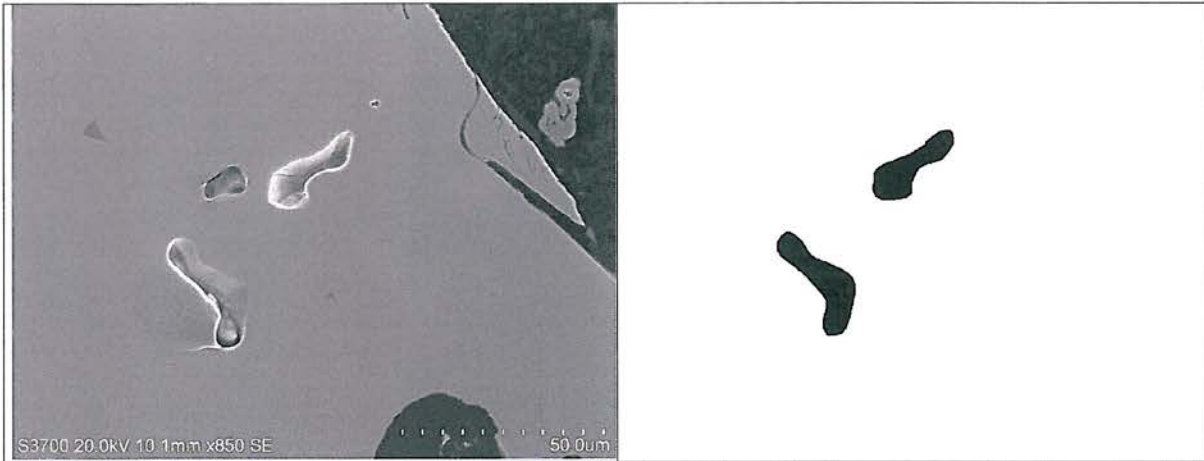
Reference sample (REF).

Figure 20. Sample REF outer area. Micro-porosity (left) and the marked porosity used for image analysis (right).
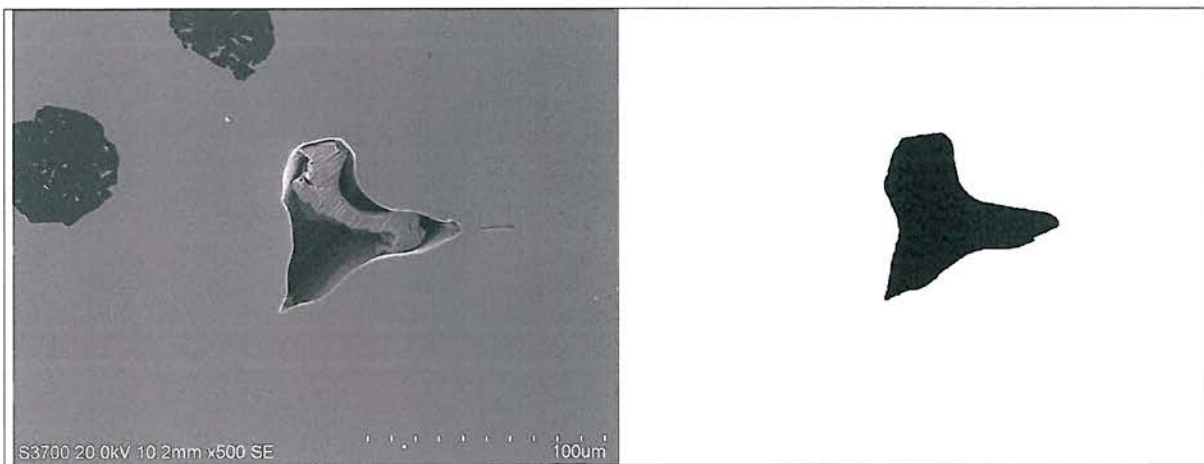

Figure 21. Sample REF, outer area. Micro-porosity (left) and the marked porosity used for image analysis (right).
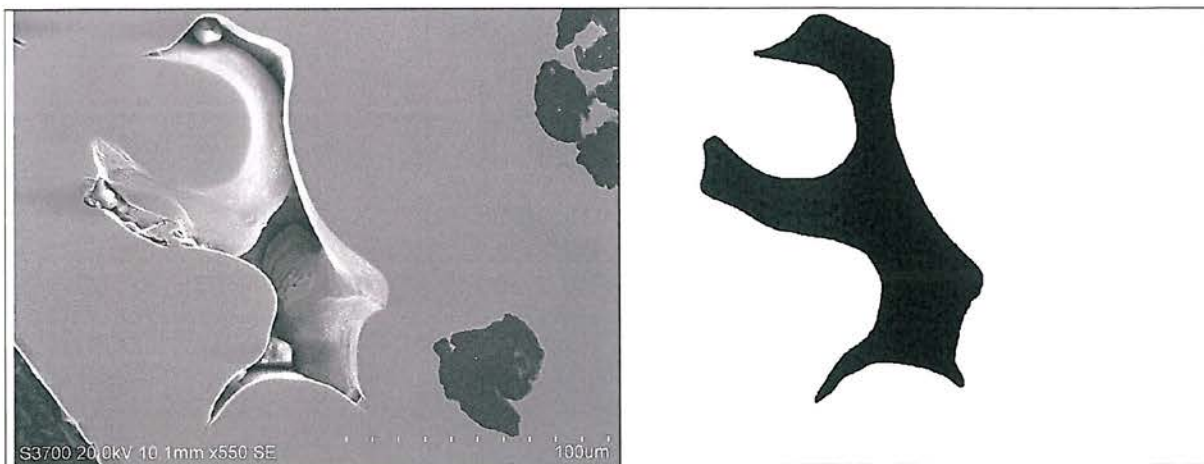

Figure 22. Sample REF, inner area. Micro-porosity (left) and the marked porosity used for image analysis (right).
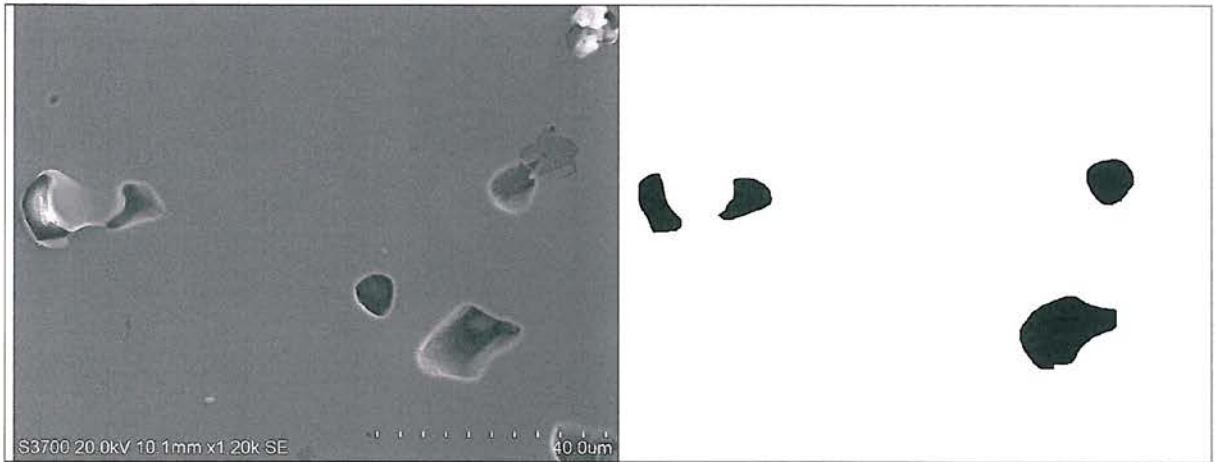
Figure 23. Sample REF, inner area. Micro-porosity (left) and the marked porosity used for image analysis (right).